



## DIPLOMARBEIT

# Simulation of High Harmonic Generation in Laser-Solid Interactions

ausgeführt am

Institut für Theoretische Physik  
der Technischen Universität Wien

---

Institute for Theoretical Physics  
Vienna University of Technology

unter der Anleitung von

Associate Prof. Dipl.-Ing. Dr.techn. Christoph Lemell  
und

O.Univ.Prof. Dipl.-Phys. Dr.rer.nat. Joachim Burgdörfer  
durch

**Isabella Floss**

Hauptstraße 121

A-2124 Kreuzstetten

[isabella.floss@tuwien.ac.at](mailto:isabella.floss@tuwien.ac.at)

---

Datum

---

Unterschrift



# Abstract

When irradiating crystalline insulators by strong and short laser pulses the non-linear response of the material gives rise to high harmonic generation (HHG). In view of compact solid-state attosecond sources and electronics at optical frequencies there is great interest from both experimentalists and theorists in understanding and explaining the underlying physical process which, however, has not been achieved so far.

We perform ab-initio simulations based on time dependent density functional theory (TDDFT) describing the ultrafast electron dynamics. In a methodological section we describe a newly developed numerical scheme to include damping (energy loss of excited electrons) and dephasing (decoherence) into TDDFT. The effects of such processes on the emission of high harmonics are discussed using a (numerically) “simple” target material, diamond. Then, we focus on the simulation of two recent experiments. We study directional dependence and relative weights of the occurring inter- and intra-band HHG from  $\text{SiO}_2$  irradiated by transients (sub-cycle pulses at optical frequencies) and we investigate the modifications of HHG spectra due to the presence of an initial excited carrier population which was motivated by pump-probe experiments on HHG from  $\text{ZnSe}$ .



# Contents

<b>1</b>	<b>Introduction</b>	<b>1</b>
<b>2</b>	<b>Method: TDDFT</b>	<b>3</b>
2.1	Structure of the code . . . . .	4
2.1.1	Ground state calculation . . . . .	4
2.1.2	Propagation of KS orbitals in real time . . . . .	7
2.2	Applications of the real time propagation . . . . .	9
2.2.1	Laser-solid interactions (beyond linear response) . . . . .	9
2.2.2	Calculation of the linear response . . . . .	16
<b>3</b>	<b>Extended Methods: beyond TDDFT</b>	<b>19</b>
3.1	Propagation effects . . . . .	19
3.2	Damping . . . . .	20
3.2.1	Phenomenological damping . . . . .	20
3.2.2	Drude friction . . . . .	25
3.3	Decoherence . . . . .	25
3.3.1	Theoretical description . . . . .	25
3.3.2	Numerical implementation in TDDFT . . . . .	28
3.3.3	First applications . . . . .	31
3.3.4	Numerical details . . . . .	37
3.3.5	Conclusions and outlook . . . . .	38
<b>4</b>	<b>HHG from <math>\alpha</math>-quartz irradiated by transients</b>	<b>39</b>
4.1	Motivation . . . . .	39
4.2	Simulation results . . . . .	40
4.2.1	Simulated crystal . . . . .	40
4.2.2	Transients on $\alpha$ -quartz . . . . .	43
4.3	Conclusions and outlook . . . . .	49

<b>5</b>	<b>Pump probe study of HHG</b>	<b>51</b>
5.1	Motivation . . . . .	51
5.2	Mid-IR pulse on ZnSe . . . . .	52
5.2.1	Simulated crystal . . . . .	52
5.2.2	Original and modified spectra . . . . .	54
5.3	Near-IR pulse on diamond . . . . .	59
5.4	Conclusions and outlook . . . . .	60
<b>6</b>	<b>Conclusions and outlook</b>	<b>65</b>
<b>7</b>	<b>Acknowledgments</b>	<b>67</b>

# 1 Introduction

The availability of laser sources providing ultrashort laser pulses with well defined electric field opened the pathway to control and manipulate electrons of atomic and extended systems. Among the non-linear processes studied intensely is the generation of high harmonic radiation, i.e., the emission of light with integer multiples of the driving field. Recently, these studies were extended to solid targets made of transparent dielectrics exploiting the extremely high target density as compared to gaseous targets [1, 2]. This achievement could be the foundation for compact solid-state attosecond sources and electronics at optical frequencies.

While high harmonic generation (HHG) in atoms can be well described with the help of the three-step model (ionization of the atom - acceleration of the released electron in the driving field - recombination under emission of an energetic photon) the mechanisms responsible for HHG in solids are still a matter of debate. Most theoretical considerations of solid HHG are based on solutions of the optical Bloch equations (OBEs) in 1D [1, 2] describing transitions of population between valence and conduction bands (interband transitions) and the acceleration of electrons/holes within the bands (intraband). To determine the relative importance of these two contributions is at the center of research. Analysis of intraband HHG might allow for an all-optical reconstruction of the target band structure. However, simulations hint at a much stronger interband HHG which might obscure intraband contributions.

In this work we do not solve the OBEs but take an alternative route to simulating HHG in solids. We model the systems using the more elaborate and reliable full 3-dimensional real-space time dependent density functional theory (TDDFT) package developed by the group of K. Yabana (University of Tsukuba) [3]. In Sec. 2 we describe an extension of this TDDFT package separating the conduction band contribution of the induced current density allowing for a better understanding of the relative roles of inter- and intraband HHG. Another extension of TDDFT is presented in Sec. 3 where

we discuss various numerical methods to implement dissipation (partly published in [4]) and decoherence processes so far not accounted for in TDDFT. The influence of the decoherence time on the HHG spectra is discussed for NIR irradiation of diamond. Finally, in Secs. 4 and 5 we model two recent experiments, HHG from  $\text{SiO}_2$  irradiated by transients [2] and a pump-probe setting with counter-propagating UV and IR laser pulses irradiating ZnSe [5]. The results are analyzed using the tools developed in Sec. 2.

Atomic units (a.u.;  $e = \hbar = m_e = 1$ ) are used throughout unless otherwise stated. Whenever arbitrary units (arb.u.) are used all subfigures within one figure correspond to the same set of arbitrary units.

## 2 Method: TDDFT

We aim at describing the coherent radiation emitted from crystalline insulators irradiated by strong and short laser pulses. The underlying non-linear electron dynamics are simulated using a real-space, real-time formulation of TDDFT [3]. The time dependent Kohn-Sham (KS) equations

$$i\partial_t\psi_i(\mathbf{r}, t) = H^{KS}(\mathbf{r}, t)\psi_i(\mathbf{r}, t) \quad (1)$$

are solved with the KS Hamiltonian

$$H^{KS}(\mathbf{r}, t) = \frac{1}{2} \left( \mathbf{p} + \frac{1}{c} \mathbf{A}(t) \right)^2 + \underbrace{V_{\text{ion}}(\mathbf{r}) + \int d^3r' \frac{n(\mathbf{r}', t)}{|\mathbf{r} - \mathbf{r}'|} + E_{\text{XC}}[n(\mathbf{r}, t)]}_{=: V_{\text{KS}}[n(\mathbf{r}, t)]} \quad (2)$$

determining the electron dynamics within one unit cell of the periodic lattice. Here,  $\mathbf{p} = -i\nabla$  denotes the momentum operator and  $\mathbf{A}(t) = -c \int_{-\infty}^t dt' \mathbf{E}(t')$  is the vector potential for a given external electric field  $\mathbf{E}(t)$ . We use the so-called “transverse” geometry, i.e., we treat an infinitely extended system along the polarization direction of the laser. Thus, we consider neither surface charges nor induced fields and the vector potential  $\mathbf{A}(t)$  is solely determined by the external laser field. Since typical wavelengths are much larger than the length  $L$  of a unit cell in a crystal (typically  $L \lesssim 1$  nm vs.  $\lambda \gtrsim 400$  nm), we assume the long wavelength limit, i.e., we apply time dependent but spatially uniform electric fields. The effective one-electron KS potential  $V_{\text{KS}}[n(\mathbf{r}, t)]$  consists of an ionic part  $V_{\text{ion}}(\mathbf{r})$  representing the combined Coulomb potential of the crystal ions and inner shell electrons which are only weakly influenced by the external time dependent potential (“frozen”), the electron-electron repulsion depending on the local electron density  $n(\mathbf{r}, t) = \sum_i N_i |\psi_i(\mathbf{r}, t)|^2$  with  $N_i$  the occupation number of the KS orbital  $\psi_i(\mathbf{r}, t)$ , and the local exchange-correlation (XC) functional  $E_{\text{XC}}[n(\mathbf{r}, t)]$  calculated using the adiabatic approximation, i.e., neglecting memory effects.

Eqs. (1) are solved in the velocity gauge making  $H^{KS}(\mathbf{r}, t)$  unit cell periodic in

space. Therefore, we may apply Bloch's theorem and introduce periodic orbitals  $u_{n\mathbf{k}}(\mathbf{r}, t)$  defined by  $\psi_i(\mathbf{r}, t) = e^{i\mathbf{k}\mathbf{r}}u_{n\mathbf{k}}(\mathbf{r}, t)$  where the index  $i$  is composed of the band index  $n$  and the crystal momentum  $\mathbf{k}$ . The time dependent KS equations thus become

$$i\partial_t u_{n\mathbf{k}}(\mathbf{r}, t) = \left\{ \frac{1}{2} \left( \mathbf{p} + \mathbf{k} + \frac{1}{c} \mathbf{A}(t) \right)^2 + V_{\text{KS}}[n(\mathbf{r}, t)] \right\} u_{n\mathbf{k}}(\mathbf{r}, t) \quad (3)$$

on a uniform Cartesian grid in real and reciprocal space. For the first and second derivatives of the orbital wave functions, we apply nine-point formulas. The time-propagation is performed using the fourth-order Taylor approximation

$$u_{n\mathbf{k}}(t + \Delta t) \simeq \sum_{m=0}^4 \frac{1}{m!} \left( -iH^{KS} \left[ \frac{n(t) + n(t + \Delta t)}{2} \right] \Delta t \right)^m u_{n\mathbf{k}}(t) \quad (4)$$

including a predictor-corrector step in the time dependent density.

## 2.1 Structure of the code

In this section, the most important features of the original TDDFT simulation (adopted from Yabana [3]) and an extension allowing for further analyzing its output are highlighted using the example of test calculations for (the numerically cheap) diamond.<sup>1</sup> We use a cuboid  $4.77 \times 4.77 \times 6.74$  a.u.<sup>3</sup> unit cell with discretization  $\Delta x_i \simeq 0.3$  a.u. in real space,  $\Delta k_i \simeq 0.06$  a.u. in reciprocal space (with  $i = 1, 2, 3$ ), and a time step of  $\Delta t = 0.02$  a.u. The inner shell  $1s^2$  electrons are frozen and included in norm-conserving pseudopotentials of the Troulliers-Martins form [6]. For the XC functional, we apply the adiabatic local-density approximation (LDA).

### 2.1.1 Ground state calculation

First, we determine the ground state (GS) of our system which is typically used as initial state for the time propagation. This is done by self-consistently solving the time

---

<sup>1</sup>In diamond the nearest neighbor distance is 2.92 a.u. and the (in-) direct band gap is 7 (5.5) eV.

independent KS equations

$$\left\{ \frac{1}{2} (\mathbf{p} + \mathbf{k})^2 + V_{\text{KS}}[n^{\text{GS}}(\mathbf{r})] \right\} u_{n\mathbf{k}}^{\text{GS}}(\mathbf{r}) = \varepsilon_{n\mathbf{k}} u_{n\mathbf{k}}^{\text{GS}}(\mathbf{r}) \quad (5)$$

on a uniform Cartesian  $\mathbf{k}$ -point grid (see Fig. 1a) applying a conjugate gradient minimization. Within each iteration step, the density is updated according to the modified Broyden method [7], i.e., only a fraction of the new density  $n_{i+1}^{\text{GS}}(\mathbf{r})$  is used for the calculation of  $V_{\text{KS}}[n^{\text{GS}}(\mathbf{r})]$ . Convergence is reached when neither density nor energy changes exceed a given limit<sup>2</sup> for a few iterations. Apart from the GS energy and the electron density (Fig. 2), we obtain the band structure (Fig. 3a) as well as the density of states (Fig. 3b) which show good agreement with corresponding calculations using VASP (Vienna Ab-initio Simulation Package [8]) and a more elaborate GGA (generalized gradient approximation) XC functional.

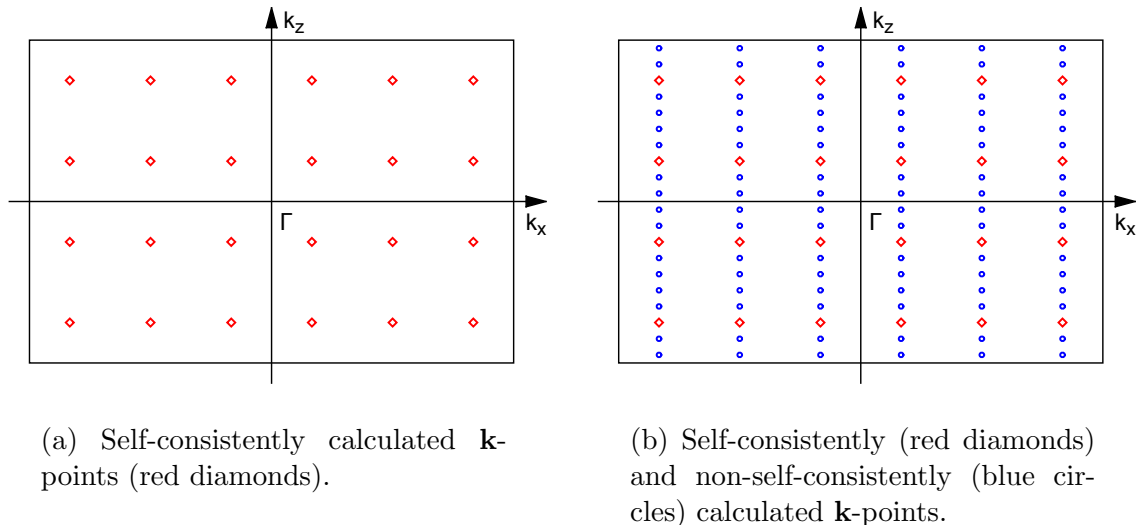


Figure 1: Scheme of  $\mathbf{k}$ -point sampling in 1<sup>st</sup> Brillouin zone.

To perform the in-depth analysis of the generated time dependent electron current we have added the optional step of refining the  $\mathbf{k}$ -grid before starting the time propagation. This is required when using the option (also set up as part of this thesis; see Sec. 2.1.2) to separate the time dependent KS orbitals into contributions of different energy bands. In order to decompose the orbitals, we project them onto Houston

<sup>2</sup>E.g.,  $\Delta E/E \lesssim 10^{-10}$  is a common convergence condition for the total energy.

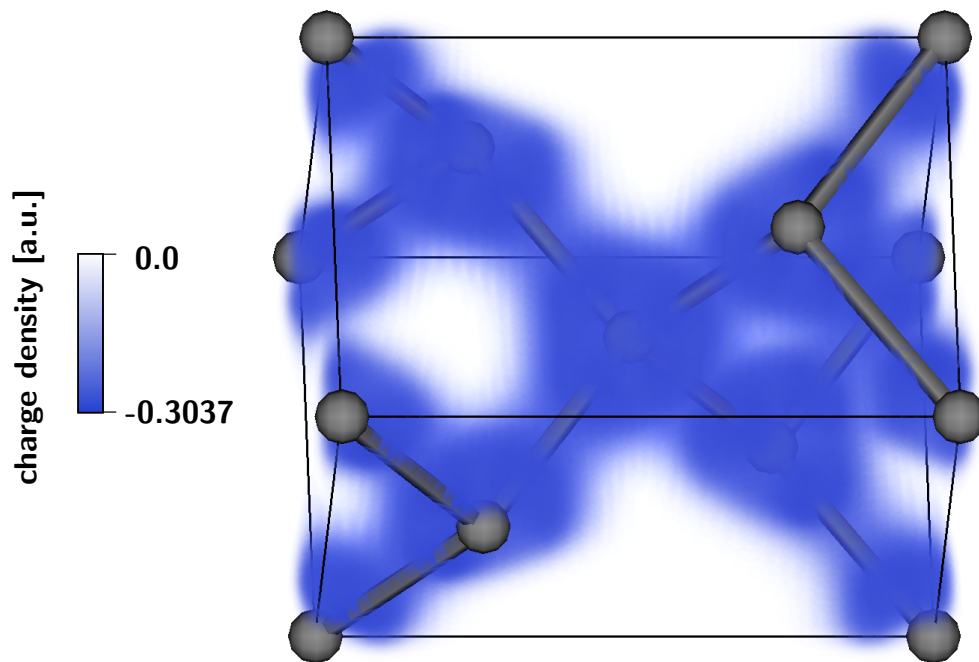


Figure 2: Volume plot of the GS electron density  $n^{\text{GS}}(\mathbf{r})$  within a diamond unit cell containing 4 carbon atoms and their periodic replicas on the unit cell boundary. ( $1s^2$  electrons are frozen and, thus, do not contribute to the density displayed here.)

states [9]

$$u_{n\mathbf{k}}^{\text{H}}(\mathbf{r}, t) = \exp\left(-i \int^t dt' \varepsilon_{n\mathbf{k}+\mathbf{A}(t')/c}\right) u_{n\mathbf{k}+\mathbf{A}(t)/c}^{\text{GS}}(\mathbf{r}) \quad (6)$$

which are the exact solutions of Eqs. (5) with an additional field  $\mathbf{A}/c$  and are applicable in the adiabatic limit, i.e., the limit of slowly varying  $\mathbf{A}(t)/c$ . Up to a global phase factor, Houston states are the solutions of the GS problem shifted by  $\mathbf{A}(t)/c$  in  $\mathbf{k}$ -space. Therefore, we have added  $\mathbf{k}$ -points only along the laser polarization direction (blue circles in Fig. 1b). At these additional  $\mathbf{k}$ -points, we solve the time-independent KS equations in order to obtain a sufficiently fine Houston basis. For this non-self-consistent calculation we use the already determined and converged GS density  $n^{\text{GS}}(\mathbf{r})$ .

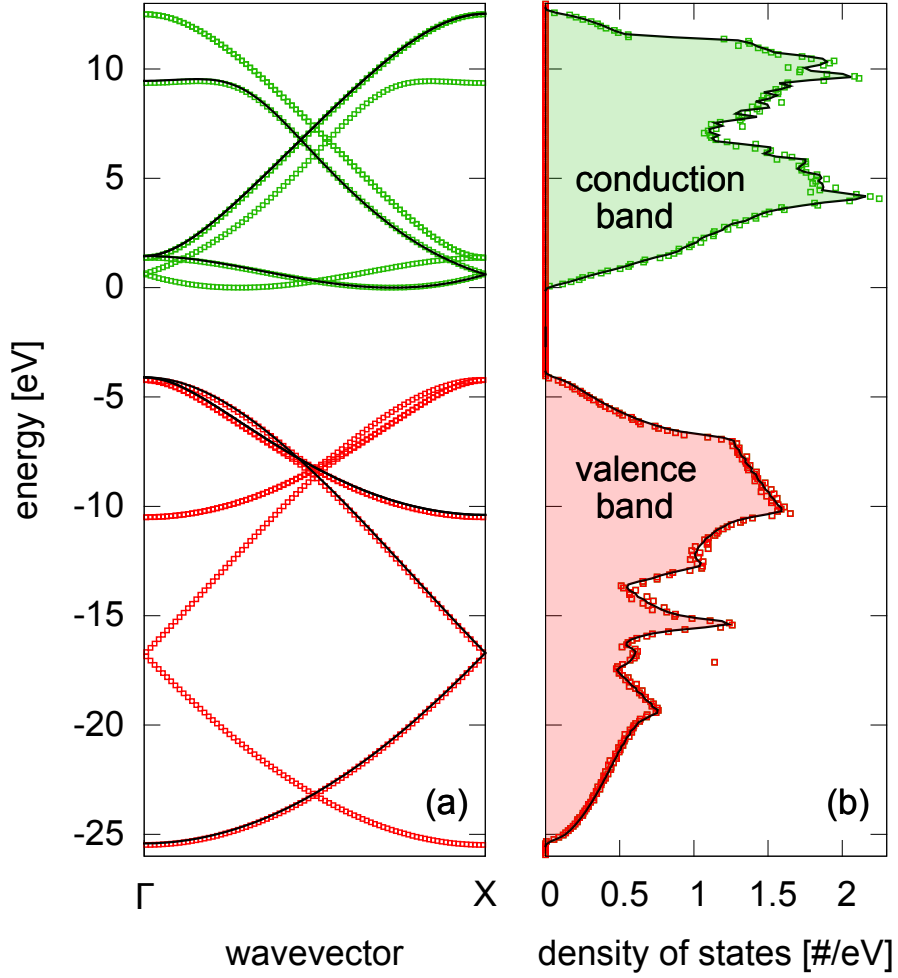


Figure 3: Simulated band structure (a) and density of states (b) of the diamond crystal. Red and green squares correspond to valence and conduction band states determined by our code, black solid lines show VASP results using a GGA XC functional.

### 2.1.2 Propagation of KS orbitals in real time

Before starting the real time calculation, we specify the external laser field by the vector potential  $\mathbf{A}(t)$ . At each time step, the KS orbitals are propagated using the 4<sup>th</sup> order Taylor approximation including a predictor-corrector step [Eq. (4)]. From the new wavefunctions the new density is computed. Together with the external vector potential  $n(\mathbf{r}, t)$  determines the new KS Hamiltonian. The output of the real time calculation is the time dependent electron density  $n(\mathbf{r}, t)$ , the induced current density

averaged over the unit cell volume  $V_c$

$$\mathbf{J}(t) = -\frac{1}{V_c} \int_{V_c} d^3r \underbrace{\sum_i \frac{N_i}{2} \left[ \psi_i^*(\mathbf{r}, t) \left( \mathbf{p} + \frac{1}{c} \mathbf{A}(t) \right) \psi_i(\mathbf{r}, t) + c.c. \right]}_{\mathbf{j}_e(\mathbf{r}, t)} + \mathbf{J}_{\text{NL}}(t) \quad (7)$$

with the non-local part  $\mathbf{J}_{\text{NL}}(t)$  coming from the non-locality of the pseudopotential and  $\mathbf{j}_e(\mathbf{r}, t)$  being the microscopic electron current density, and the total energy of the system as functions of time.

Optionally, the time dependent KS orbitals can be expanded into Houston states  $|\psi_{n\mathbf{k}}^{\text{H}}\rangle = |\psi_{n\mathbf{k}'}^{\text{GS}}\rangle$  on the refined  $\mathbf{k}$ -grid at times for which the system is closest to one of the additional points

$$\mathbf{k}' = \mathbf{k} + \frac{1}{c} \mathbf{A}(t) + \mathbf{G} \quad (8)$$

with  $\mathbf{G}$  an arbitrary reciprocal lattice vector. The decomposition

$$|\psi_{n\mathbf{k}}(t)\rangle = \sum_m c_{mn}^{\mathbf{k}}(t) |\psi_{m\mathbf{k}}^{\text{H}}\rangle \quad (9)$$

is done by computing the coefficients

$$c_{mn}^{\mathbf{k}}(t) = \langle \psi_{m\mathbf{k}}^{\text{H}} | \psi_{n\mathbf{k}}(t) \rangle. \quad (10)$$

With this, the orbitals can be separated into valence band

$$|\psi_{n\mathbf{k}}^{\text{vb}}(t)\rangle = \sum_{m=1}^{N^{\text{vb}}} c_{mn}^{\mathbf{k}}(t) |\psi_{m\mathbf{k}}^{\text{H}}\rangle \quad (11)$$

where  $N^{\text{vb}}$  is the number of valence bands, and conduction band contributions

$$|\psi_{n\mathbf{k}}^{\text{cb}}(t)\rangle = |\psi_{n\mathbf{k}}(t)\rangle - |\psi_{n\mathbf{k}}^{\text{vb}}(t)\rangle. \quad (12)$$

Accordingly, the electron density can be split into valence and conduction band contributions. Using Eq. (12) we calculate the intraband current defined in this work as

the current within the conduction band

$$\mathbf{J}^{\text{ra}}(t) = -\frac{1}{V_c} \int_{V_c} d^3r \sum_i \frac{N_i}{2} \left[ \psi_i^{\text{cb}*}(\mathbf{r}, t) \left( \mathbf{p} + \frac{1}{c} \mathbf{A}(t) \right) \psi_i^{\text{cb}}(\mathbf{r}, t) + c.c. \right] + \mathbf{J}_{\text{NL}}^{\text{cb}}(t). \quad (13)$$

The remaining part of the total current  $\mathbf{J}(t)$  determines the interband current

$$\mathbf{J}^{\text{er}}(t) = \mathbf{J}(t) - \mathbf{J}^{\text{ra}}(t). \quad (14)$$

Since, at present, a further separation of the remaining part into contributions within the valence band and between valence and conduction bands is numerically unstable<sup>3</sup>, we stick to the definitions for  $\mathbf{J}^{\text{ra}}(t)$  and  $\mathbf{J}^{\text{er}}(t)$  given in Eqs. (13) and (14).

## 2.2 Applications of the real time propagation

There are two modes of the real time calculation for which the shape of the external field differ significantly.

### 2.2.1 Laser-solid interactions (beyond linear response)

A (few-cycle) laser pulse of the form  $\mathbf{E}(t) \sim \mathbf{E}_0(t) \cos(\omega_L t + \phi_{\text{CE}})$  with envelope  $\mathbf{E}_0(t)$ , laser frequency  $\omega_L$ , and carrier-envelope phase  $\phi_{\text{CE}}$  is interacting with the electronic system of the unit cell. In order to clearly demonstrate non-linear effects, we choose a rather intense few-cycle laser pulse ( $I_{\text{max}} = 2 \times 10^{13}$  W/cm<sup>2</sup>; Fig. 4a) with polarization along the  $\Gamma$ -X direction (Fig. 3) for a test simulation. Performing the real time calculation, we obtain the time dependent density, current density, and total energy of the system. Apart from non-linear effects that appear mostly in the second half of the pulse and are difficult to explain, the simulation results support the following physical picture (Fig. 4): The electric field (Fig. 4a) is responsible for the population of the conduction band. Therefore, conduction band population and electronic excitation energy show oscillations with maxima almost coinciding with the extrema of the

---

<sup>3</sup>The origin of these instabilities will be subject of future investigations.

input electric field i.e. the maxima of the excitation rate (Fig. 4d). Conversely, inter- and intraband contributions of the induced current density have a phase shift of  $\pm\pi/2$  relative to the electric field (Fig. 4b) which can be understood as follows: The linear response contribution of the interband current is given by the motion of the bound electrons. The displacement  $\mathbf{r}(t)$  of a bound charge is in phase with the applied force  $\mathbf{F}(t) = q\mathbf{E}(t)$ . Thus, the resulting current density  $\mathbf{J}^{\text{er}}(t) \propto q\dot{\mathbf{r}}(t) \propto \dot{\mathbf{E}}(t)$  shows a phase shift of  $\pi/2$  relative to the electric field. In contrast, the intraband current results from the motion of the excited carriers in the conduction band. They follow the external force almost like free carriers  $\ddot{\mathbf{r}}(t) \propto \mathbf{F}(t)$  resulting in a phase shift of  $-\pi/2$  between the intraband current and the applied electric field  $\mathbf{J}^{\text{ra}}(t) \propto q\dot{\mathbf{r}}(t) \propto \int \mathbf{E}(t) dt$ .

Furthermore, we get first impressions of the spatial distribution of the induced charge densities. During the laser pulse the total induced charge density  $\rho(\mathbf{r}, t) - \rho^{\text{GS}}(\mathbf{r})$  is dominated by periodic oscillations (Fig. 5). Surprisingly, the conduction band density is strongly localized around the atoms. It forms a “doughnut-shaped” distribution (Fig. 6) growing and shrinking within each laser half-cycle and finally staying in the conduction band after irradiation. Compared to the ground state density, after the pulse there is slightly less electron density located along the atomic bonds (indicated by regions of positive induced charge density in Fig. 7).

Finally, we can calculate the transferred charge

$$Q_{\text{L}} = \mathbf{P}(t > \tau_{\text{p}}) \cdot \mathcal{A}_{\text{eff}} \quad (15)$$

from the polarization density

$$\mathbf{P}(t) = \int_{-\infty}^t dt' \mathbf{J}(t') \quad (16)$$

at the end of the pulse and the effective surface area perpendicular to the laser polarization direction  $\mathcal{A}_{\text{eff}}$ . Note that the transferred charge strongly depends on both

inter- and intraband contributions of the polarization density (Fig. 4c).

As we are interested in the simulation of HHG spectra emitted from dielectrics irradiated by short laser pulses, we determine the spectral density of the emitted intensity with polarization direction  $\hat{n}$  by Larmor's formula [10]

$$S_{\hat{n}}(\omega) \propto \left| \mathfrak{Ft} \left\{ \frac{d}{dt} \mathbf{J}(t) \cdot \hat{n} \right\} \right|^2 = \omega^2 \left| \int dt e^{i\omega t} \mathbf{J}(t) \cdot \hat{n} \right|^2. \quad (17)$$

Again, we split the spectrum into inter-

$$S_{\hat{n}}^{\text{er}}(\omega) \propto \left| \mathfrak{Ft} \left\{ \frac{d}{dt} \mathbf{J}^{\text{er}}(t) \cdot \hat{n} \right\} \right|^2 \quad (18)$$

and intraband contributions

$$S_{\hat{n}}^{\text{ra}}(\omega) \propto \left| \mathfrak{Ft} \left\{ \frac{d}{dt} \mathbf{J}^{\text{ra}}(t) \cdot \hat{n} \right\} \right|^2. \quad (19)$$

Note, that in general  $S_{\hat{n}}^{\text{er}}(\omega) + S_{\hat{n}}^{\text{ra}}(\omega) \neq S_{\hat{n}}(\omega)$ . The intraband spectrum is typically much less intense than the interband spectrum (Fig. 8). Furthermore, clear maxima at harmonic frequencies<sup>4</sup>  $(2n + 1)\omega_L$  (dotted lines in Fig. 8) are found only in the first part of the pulse (Fig. 8a). Close to the end of the pulse, a noisy spectrum is generated (Fig. 8c) which is directly related to the rather high noise level in the induced current density at the end of the pulse (Fig. 4b). Emission of the highest harmonics is observed after the maximum of the laser pulse (Figs. 8b and c).

---

<sup>4</sup>Due to the inversion symmetry of diamond, we would expect only odd harmonics for irradiation by a laser pulse containing as many cycles as the one used (Fig. 4a).

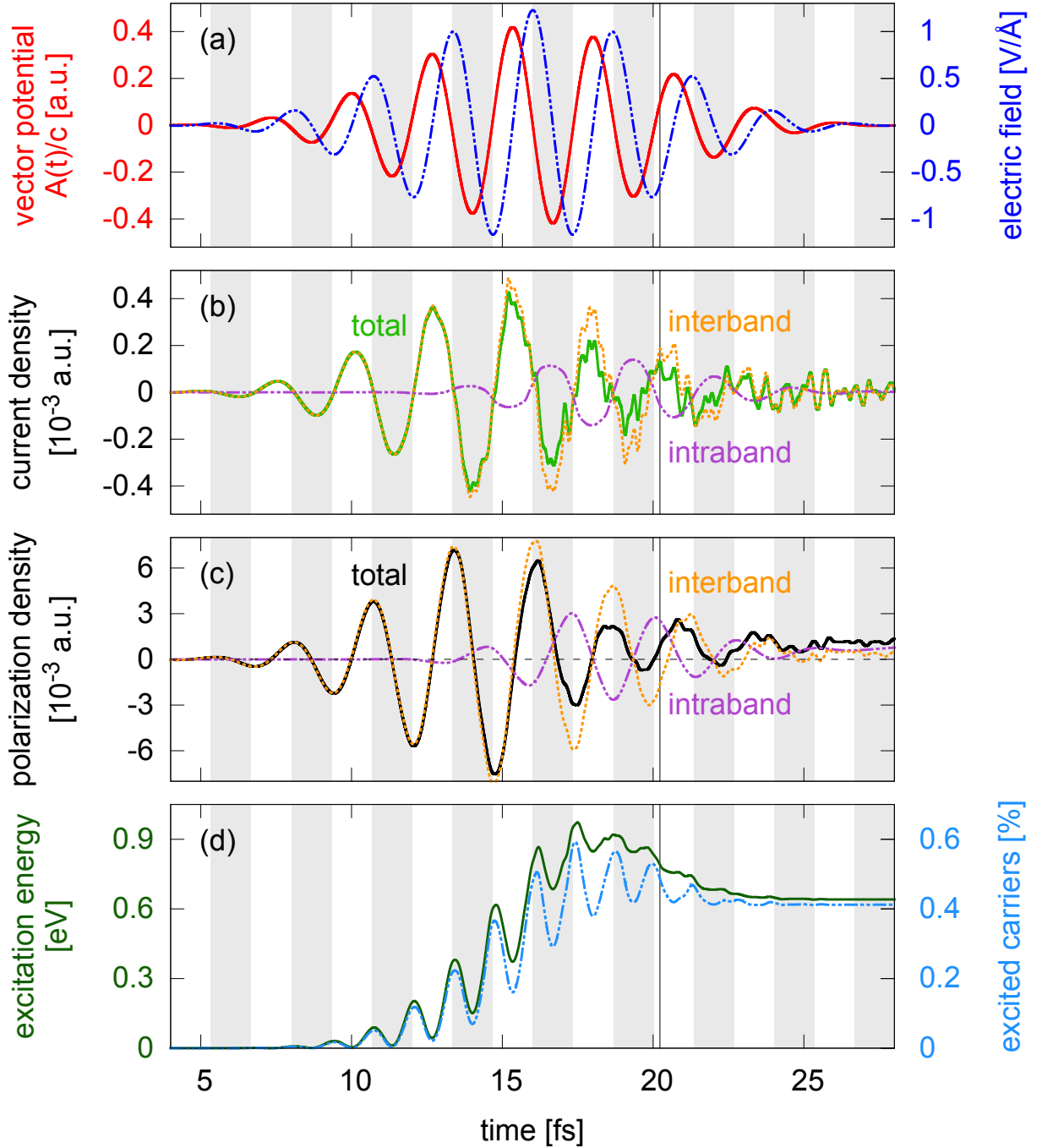


Figure 4: (a) Electric field with a  $\cos^6$ -envelope, peak intensity  $I_{\max} = 2 \times 10^{13} \text{ W/cm}^2$ ,  $\hbar\omega_L = 1.55 \text{ eV}$ , and  $\phi_{\text{CE}} = 0$  (blue), and the corresponding input vector potential  $\mathbf{A}(t)/c$  (red). (b) Induced current density along the laser polarization direction (green), and decomposition into intraband (purple) and interband (orange) contributions. (c) Induced polarization density along the laser polarization direction (black), and decomposition into intraband (purple) and interband (orange) contributions. (d) Excitation energy within one unit cell (including 4 carbon atoms) (dark-green), and occupation of conduction band (blue). The vertical lines in (a-d) correspond to the point in time chosen for Figs. 5-6.

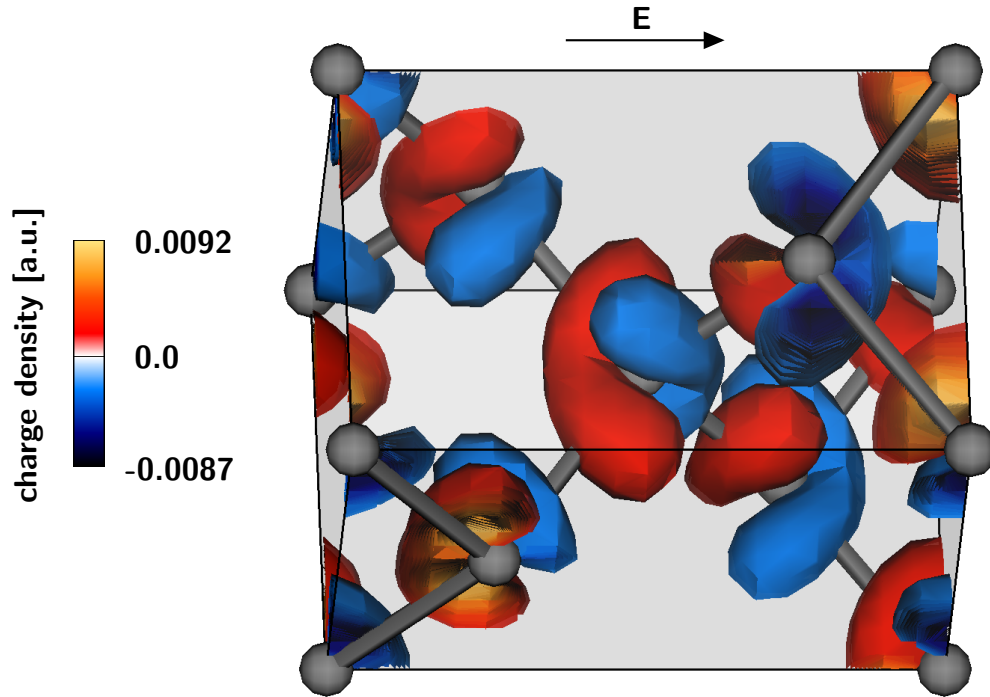


Figure 5: Isosurface plot of the induced charge density  $\rho(\mathbf{r}, t) - \rho^{\text{GS}}(\mathbf{r})$  at  $t \simeq 20.2$  fs. The outermost red (blue) surface corresponds to a charge density of  $(-)$ 0.0025 a.u.

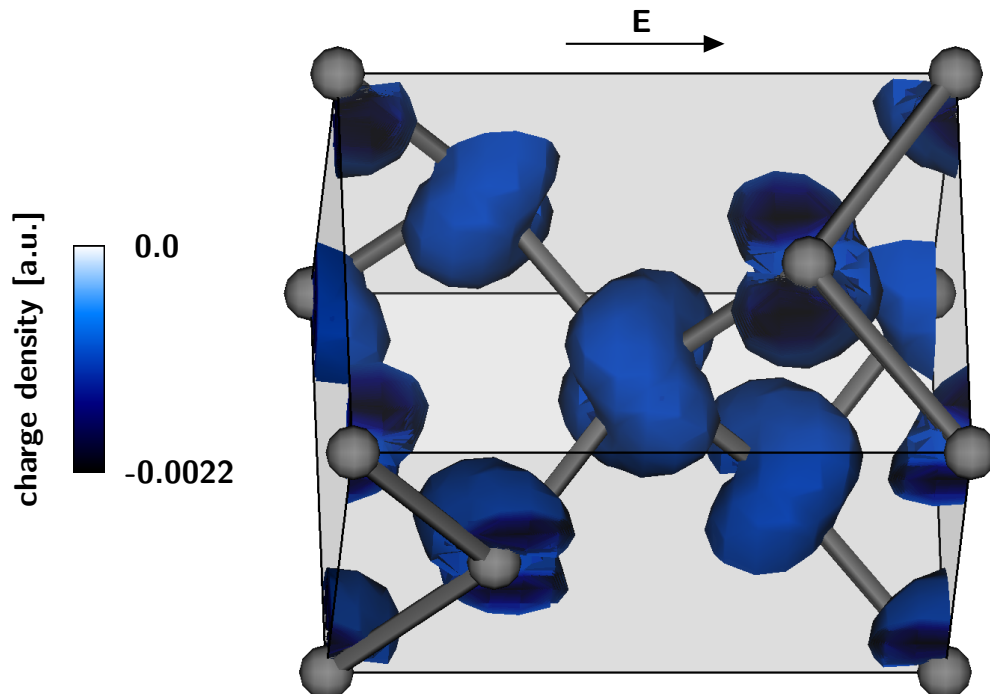


Figure 6: Isosurface plot of the conduction band charge density  $\rho^{\text{cb}}(\mathbf{r}, t)$  at  $t \simeq 20.2$  fs. The outermost surface corresponds to a charge density of -0.0011 a.u.

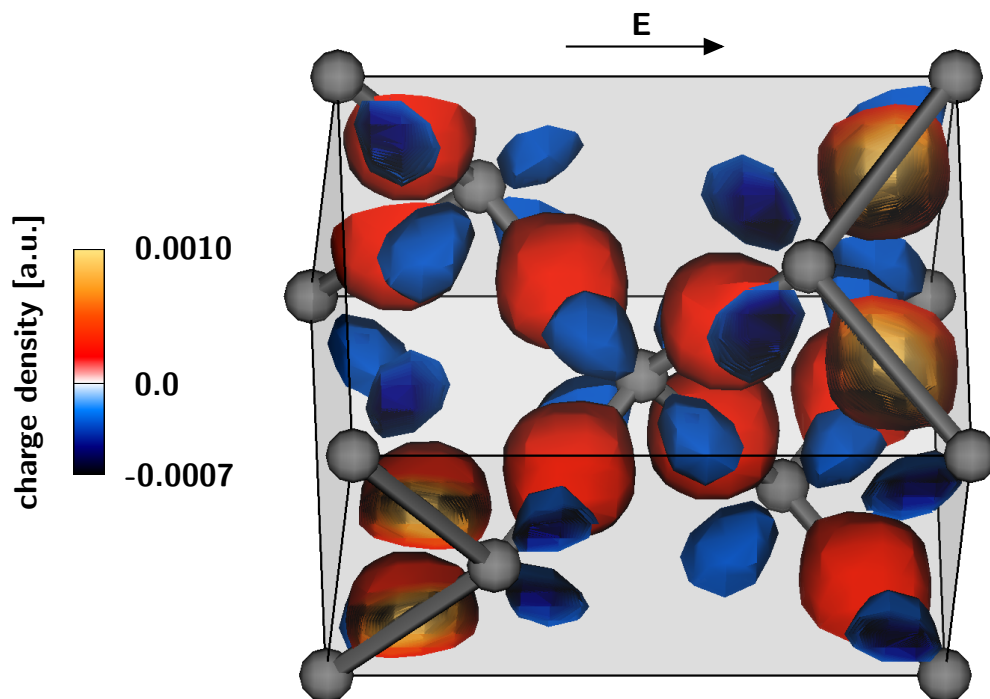


Figure 7: Isosurface plot of the induced charge density  $\rho(\mathbf{r}, t) - \rho^{\text{GS}}(\mathbf{r})$  after the pulse (at  $t \simeq 33.8$  fs). The outermost red (blue) surface corresponds to a charge density of (-)0.0003 a.u.

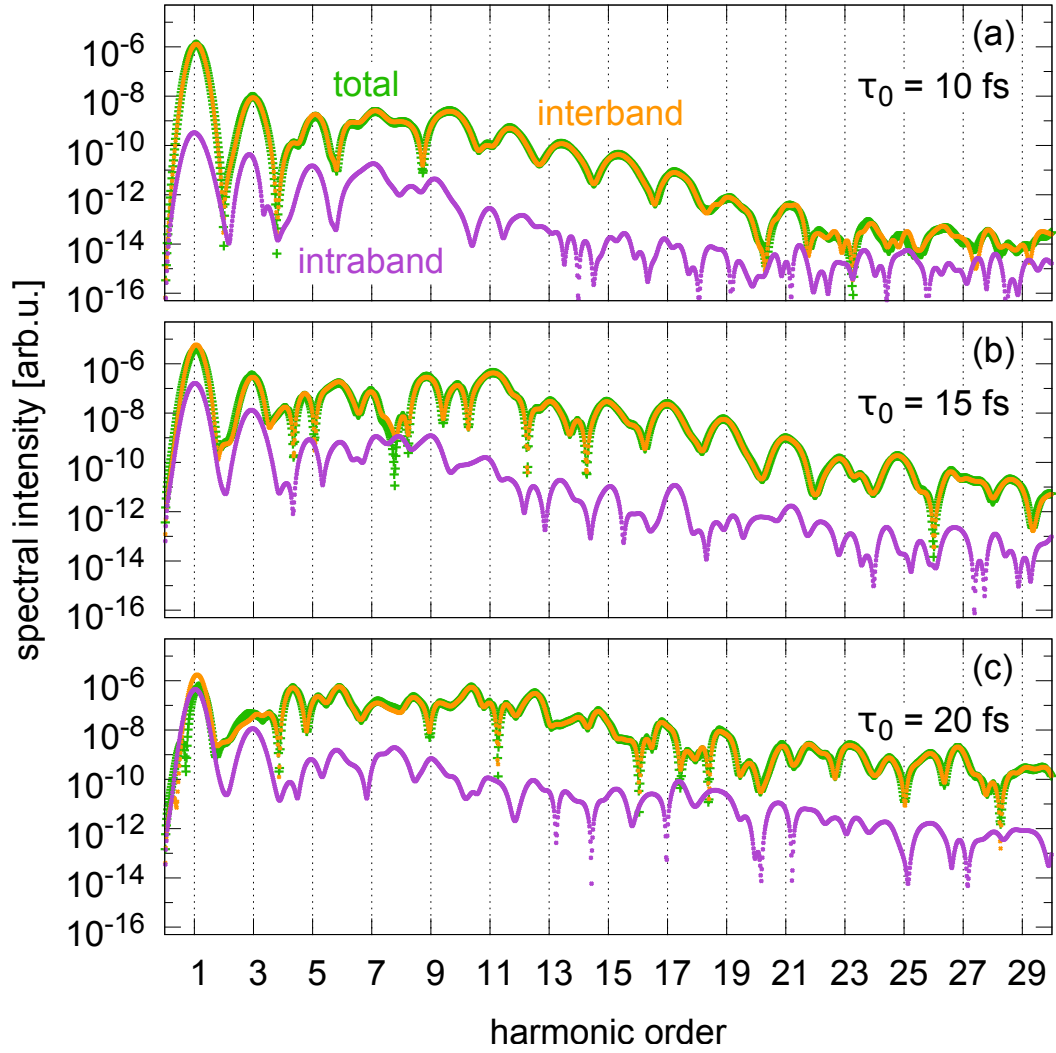


Figure 8: Total (green), interband (orange), and intraband (purple) HHG spectra induced by the laser pulse given in Fig. 4a. For the Fourier transform of the current, we use a Gaussian window function with a width of  $\sigma_t = 2$  fs centered around  $\tau_0 = 10$  fs (a),  $\tau_0 = 15$  fs (b), and  $\tau_0 = 20$  fs (c).

## 2.2.2 Calculation of the linear response

The dielectric function  $\varepsilon(\omega)$  describes the response of the system to an external excitation with frequency  $\omega$ .  $\varepsilon(\omega)$  can be derived from a single simulation if the system is uniformly and simultaneously excited at all frequencies. This is achieved by choosing a step function as input vector potential

$$\mathbf{A}(t) = \mathbf{A}_0\theta(t) \quad (20)$$

which corresponds to a  $\delta$ -shaped electric field which, in turn, is constant in frequency space

$$\mathbf{E}(t) = -\frac{1}{c} \frac{d\mathbf{A}(t)}{dt} = -\frac{\mathbf{A}_0}{c} \delta(t) = -\mathbf{F}_0 \int e^{i\omega t} d\omega. \quad (21)$$

In order to stay within the regime of linear response, we choose a rather small vector potential step (in our test calculation  $|\mathbf{A}_0|/c \simeq 0.002$  a.u.). Applying Ohm's law, we calculate the conductivity

$$\sigma(\omega) = -cJ(\omega)/A_0 \quad (22)$$

and from  $\sigma(\omega)$  the dielectric function

$$\varepsilon(\omega) = 1 + \frac{4\pi i\sigma(\omega)}{\omega} \quad (23)$$

using  $J(\omega)$ , the Fourier transform of the induced current density component parallel to the polarization direction. At the end of the calculation ( $t = \tau_e$  with typically  $\tau_e \lesssim 20$  fs) unphysical oscillations<sup>5</sup> are observed which can be damped by multiplying  $J(t)$  with a smoothing function, e.g.,

$$f_{\text{smooth}}(t) = 1 - 3 \left( \frac{t}{\tau_e} \right)^2 + 2 \left( \frac{t}{\tau_e} \right)^3 \quad (24)$$

(Fig. 9) before computing  $J(\omega)$  by the Fourier transformation

---

<sup>5</sup>The origin of these oscillations and a method to suppress them is discussed in detail in Sec. 3.3.

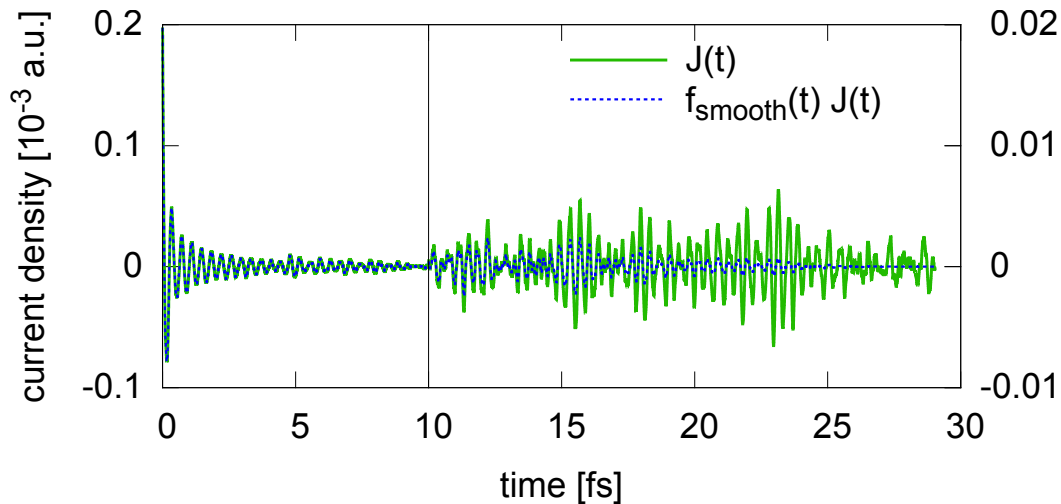


Figure 9: Induced current density before (green) and after (blue) multiplication with the smoothing function (24).

$$J(\omega) = \int_0^{\tau_e} dt e^{i\omega t} f_{\text{smooth}}(t) J(t). \quad (25)$$

For the choice of (24), still, small oscillations remain in  $\sigma(\omega)$  and  $\varepsilon(\omega)$  (Fig. 10). Comparing calculated and measured dielectric functions we find the well-known reduction of the band gap due to the choice of the LDA XC functional (Fig. 10b). Furthermore, we observe a singularity of  $\varepsilon(\omega = 0)$  due to the violation of the translational invariance in the real-space grid calculation [12]. It is closely related to a small offset in the induced current density occurring at the end of the linear response calculation. Still, for  $\omega > 0$  experimental and simulation results agree quite well.

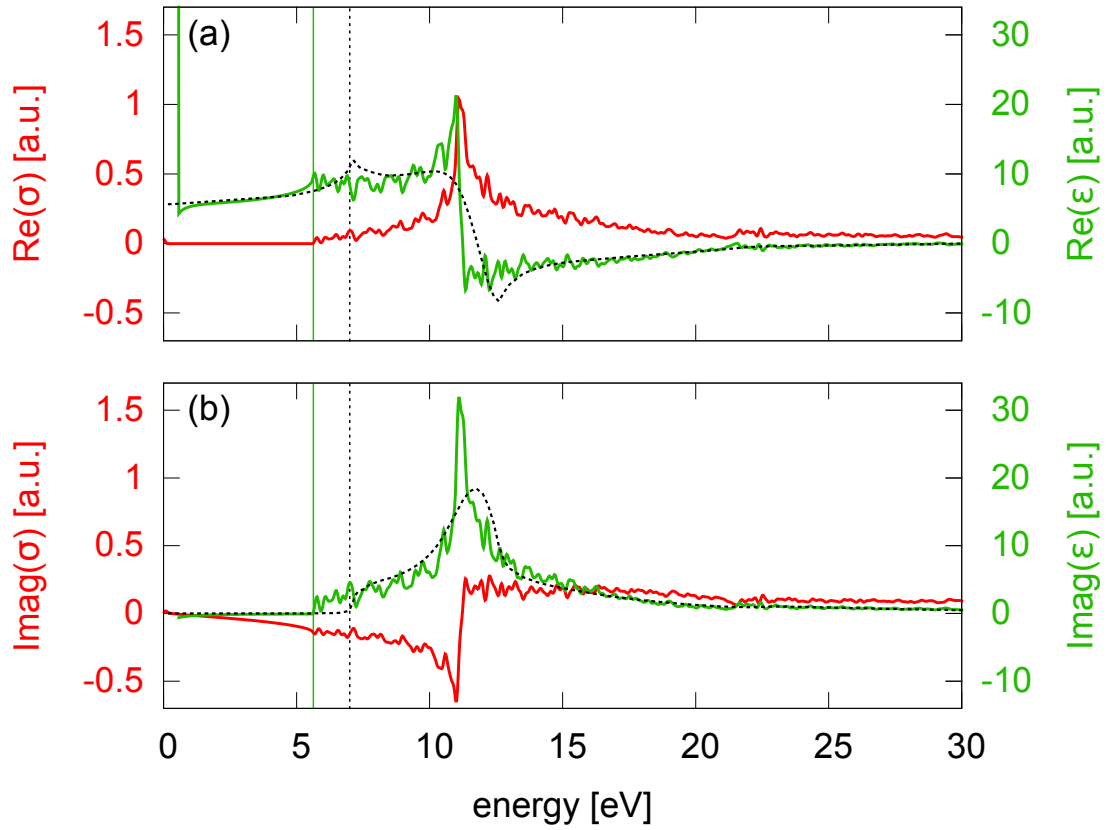


Figure 10: Real (a) and imaginary (b) parts of the conductivity (solid red) and the dielectric function (solid green) of diamond computed in a response calculation, and the measured dielectric function [11] (dashed black). The vertical lines indicate experimental (dashed black) and LDA (solid green) band gaps.

### 3 Extended Methods: beyond TDDFT

When describing experiments on crystals irradiated by short laser pulses via TDDFT simulations, there are several problems to be considered: Due to the approximations in the XC functional the exact form of which is unknown, many-body effects are not fully taken into account. Within the adiabatic approximation memory effects are not treated at all. At present, however, only adiabatic functionals are available. Research on  $E_{XC}$  including memory effects is still in its infancy. Neither dissipative nor coherence-loss processes such as electron-electron or electron-phonon scattering are included in TDDFT. Furthermore, when considering a single unit cell of the crystal, surface and propagation effects are completely neglected. In the following, we discuss several methods to improve TDDFT to account for energy-loss and decoherence processes. Propagation effects are included by a mixed micro- and macroscopic simulation scheme.

#### 3.1 Propagation effects

Including propagation effects is based on treating the coupled dynamics of electrons and electromagnetic fields. For this multiscale simulation, the time dependent KS equations (1) describing the microscopic electron dynamics and Maxwell's equations (using the transverse gauge  $\nabla \cdot \mathbf{A}(\mathbf{r}, t) = 0$ )

$$\frac{1}{c^2} \frac{\partial^2 \mathbf{A}(X, t)}{\partial t^2} - \frac{\partial^2 \mathbf{A}(X, t)}{\partial X^2} = \frac{4\pi}{c} \mathbf{J}(X, t) \quad (26)$$

for the electromagnetic field are solved simultaneously. Here,  $X$  denotes the macroscopic coordinate along the laser pulse propagation direction ( $x$  in Fig. 11). Each macroscopic grid point  $X_i$  within the crystal corresponds to one TDDFT unit cell.

The procedure briefly described above (details are provided in [12]) is an established but numerically very expensive method to include propagation effects. This multiscale method has not been used within this thesis but should be used in future investigations when comparing with experimental data.

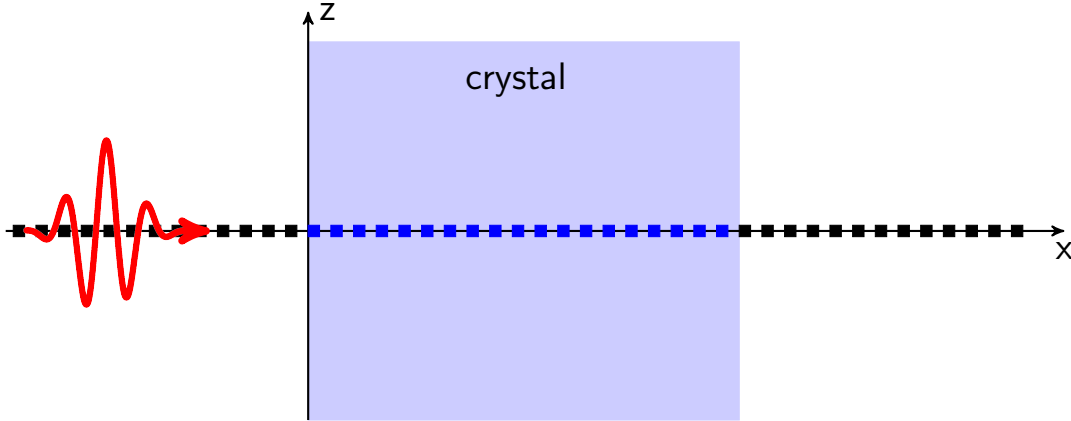


Figure 11: Illustration of the multiscale system. A laser pulse (red) irradiates a crystal (blue). Space is discretized by macroscopic grid points (filled squares). Within the crystal each macroscopic grid point (blue squares) corresponds in addition to a single TDDFT cell.

## 3.2 Damping

In conventional TDDFT no dissipative processes such as electron-hole recombination or inelastic scattering events are included. Therefore, an excited system has no possibility to lose its excitation energy. In the following we discuss methods to reduce the excitation energy and, as a consequence, the induced current density of the simulated system.

### 3.2.1 Phenomenological damping

A simple way of lowering the excitation energy of the system is to reduce the number of excited particles. This can be achieved by an additional step of decreasing the conduction band population<sup>6</sup>

$$|\tilde{\psi}_{n\mathbf{k}}^{\text{cb}}(t + \Delta t)\rangle \simeq e^{-\alpha_{\text{ph}}(H^{\text{KS}} - E_0)\Delta t} |\psi_{n\mathbf{k}}^{\text{cb}}(t + \Delta t)\rangle \quad (27)$$

in the time propagation (4). Here,  $\alpha_{\text{ph}}$  determines the phenomenological damping constant and  $E_0$  serves as reference energy level. In order to guarantee a reduction of

<sup>6</sup>For this very first attempt to include damping, we do not redistribute the damped population leading to the violation of charge conservation.

the excitation energy, the lowest level of the conduction band  $E_{\text{bottom}(\text{cb})}$  is an upper bound for  $E_0$ .

From calculations for the test system diamond (details in Sec. 2.1) using the highest level of the valence band (VB) as reference energy ( $E_0 = E_{\text{top}(\text{vb})}$ ), we observe that the number of excited carriers and, therefore, the excitation energy is reduced. Especially for short phenomenological damping times<sup>7</sup>  $\tau_{\text{ph}} \gtrsim 2$  fs, also the noisy oscillations in the induced current density after the laser pulse disappear quickly (Fig. 12). Since most conduction band (CB) electrons are removed from the system shortly after their creation, the intraband (i.e. conduction band) contribution to the current density is considerably reduced (Fig. 12c). Therefore, the total current density is dominated by the (remaining) interband contribution. Note that reducing the number of CB electrons indirectly leads to a decrease in VB population. This might at first seem counter-intuitive but can be understood as follows: also the transient CB population is partly removed before it is transferred back into the VB which results in a reduced VB population (Fig. 12d).

First, we analyze the interband current which dominates the total current in this example. In this work, it is given by the *real* interband current between VB and CB plus the hole current within the VB (cf. Eq. (14)). Since the motion of a hole in the VB (apart from its smaller velocity and oscillation amplitude due to typically larger effective masses) is similar to the motion of CB electrons, VB and CB currents (opposite sign of charge and opposite direction of motion) are in phase and have a phase shift of  $\pi$  to the *real* interband (i.e. polarization) current (cf. discussion in Sec. 2.2.1). Within the present approximation short damping times  $\tau_{\text{ph}}$  lead to increased hole densities and, thus, hole currents which result in a phase shift in the interband and, conse-

---

<sup>7</sup>Here, the damping time  $\tau_{\text{ph}}$  depends on the eigenenergy  $\varepsilon_{m\mathbf{k}}^{\text{H}}$  of the considered component  $c_{mn}^{\mathbf{k}}(t)|\psi_{m\mathbf{k}}^{\text{H}}\rangle$  of the conduction band wavefunction  $|\psi_{n\mathbf{k}}^{\text{cb}}(t)\rangle$ . Larger  $\varepsilon_{m\mathbf{k}}^{\text{H}}$  means shorter damping times where  $\tau_{\text{ph}}$  is defined as damping time of the lowest conduction band state, i.e.,

$$\alpha_{\text{ph}} = \frac{1}{(E_{\text{bottom}(\text{cb})} - E_{\text{top}(\text{vb})})\tau_{\text{ph}}}. \quad (28)$$

quently, total currents (Fig. 12b). Furthermore, imposing phenomenological damping modifies the shape of the harmonic spectra. A much clearer structure of the expected odd harmonics (indicated by dotted lines in Fig. 13) emerges for total, inter- as well as intraband spectra. When reducing the CB part of the wavefunction, obviously also coherences between CB and VB parts are damped. A different method to account for loss of coherence is discussed in Sec. 3.3.

Phenomenological damping is a simple way to reduce the energy of the system but encounters several problems: since the particle number is not conserved, the KS wavefunctions are no longer orthonormal. So far, physically meaningful methods to redistribute the damped population to lower lying states are not easily accessible. (When just renormalizing the damped KS wavefunctions, the Pauli exclusion principle is violated.) Furthermore, the energy dependence of the damping term and the damping time  $\tau_{\text{ph}}$  can only be roughly estimated. E.g., one possibility for improvement would be a velocity dependent damping time  $\tau_{\text{ph}} \propto \frac{\lambda_{\text{in}}}{v_{\text{g}}}$  indirectly proportional to the group velocity  $v_{\text{g}}$  with the inelastic mean free path  $\lambda_{\text{in}}$ . Since the calculation of  $v_{\text{g}}$  would involve great programming effort, this improvement is not considered here. Finally, the presented phenomenological damping method provides only a first glimpse at possible effects of coherence loss and dissipative processes.

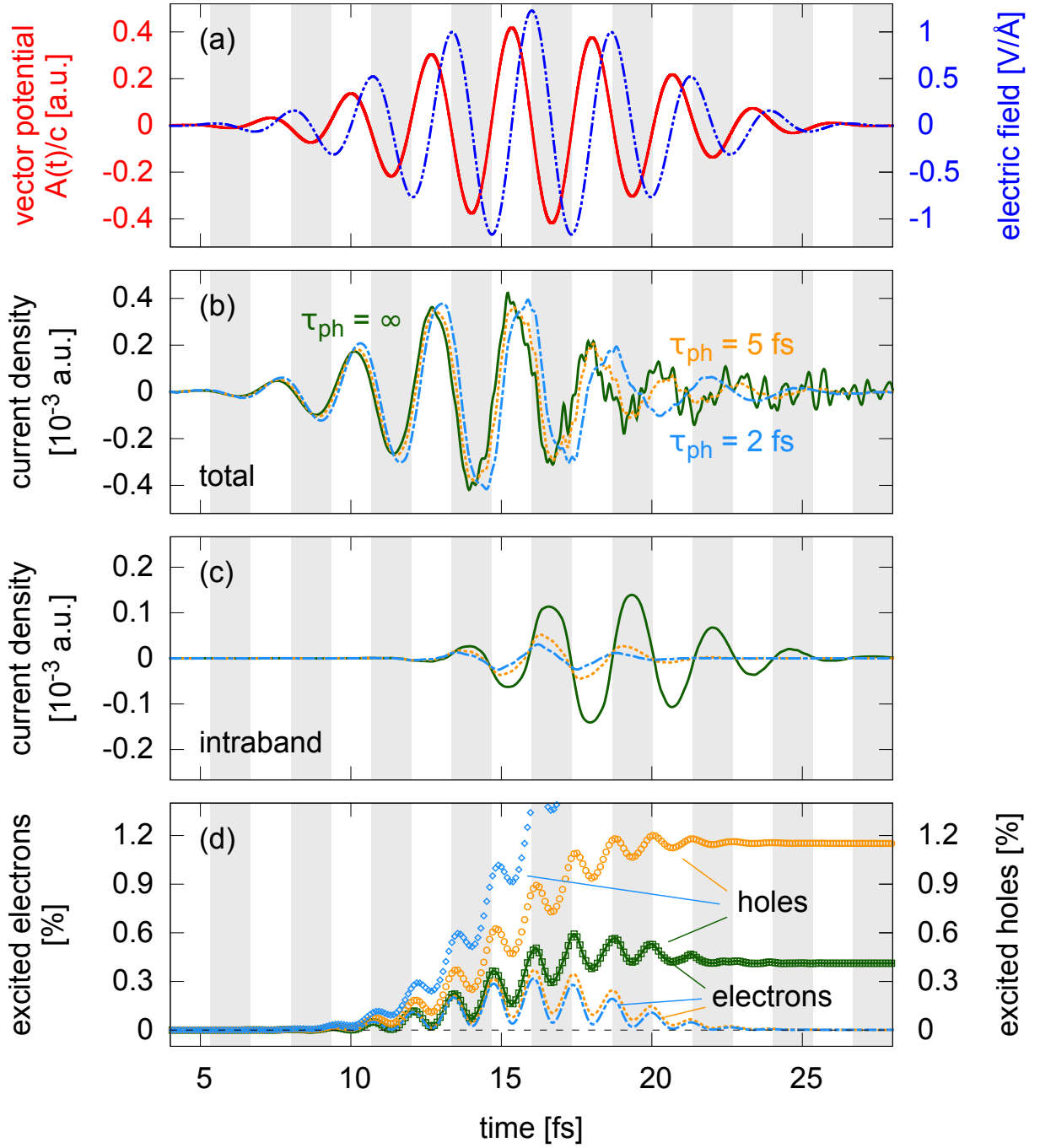


Figure 12: (a) Electric field with a  $\cos^6$ -envelope, peak intensity  $I_{\max} = 2 \times 10^{13} \text{ W/cm}^2$ ,  $\hbar\omega_L = 1.55 \text{ eV}$ , and  $\phi_{CE} = 0$  (blue), and the corresponding input vector potential  $\mathbf{A}(t)/c$  (red) (same pulse as in Sec. 2.2.1). (b-d) Induced total (b) and intraband (c) current densities along the laser polarization direction, and the occupation of CB (lines) and VB (dots) states (d) as functions of time. Green, orange, and blue curves correspond to phenomenological damping times of  $\tau_{ph} = \infty$ ,  $\tau_{ph} = 5 \text{ fs}$ , and  $\tau_{ph} = 2 \text{ fs}$ .

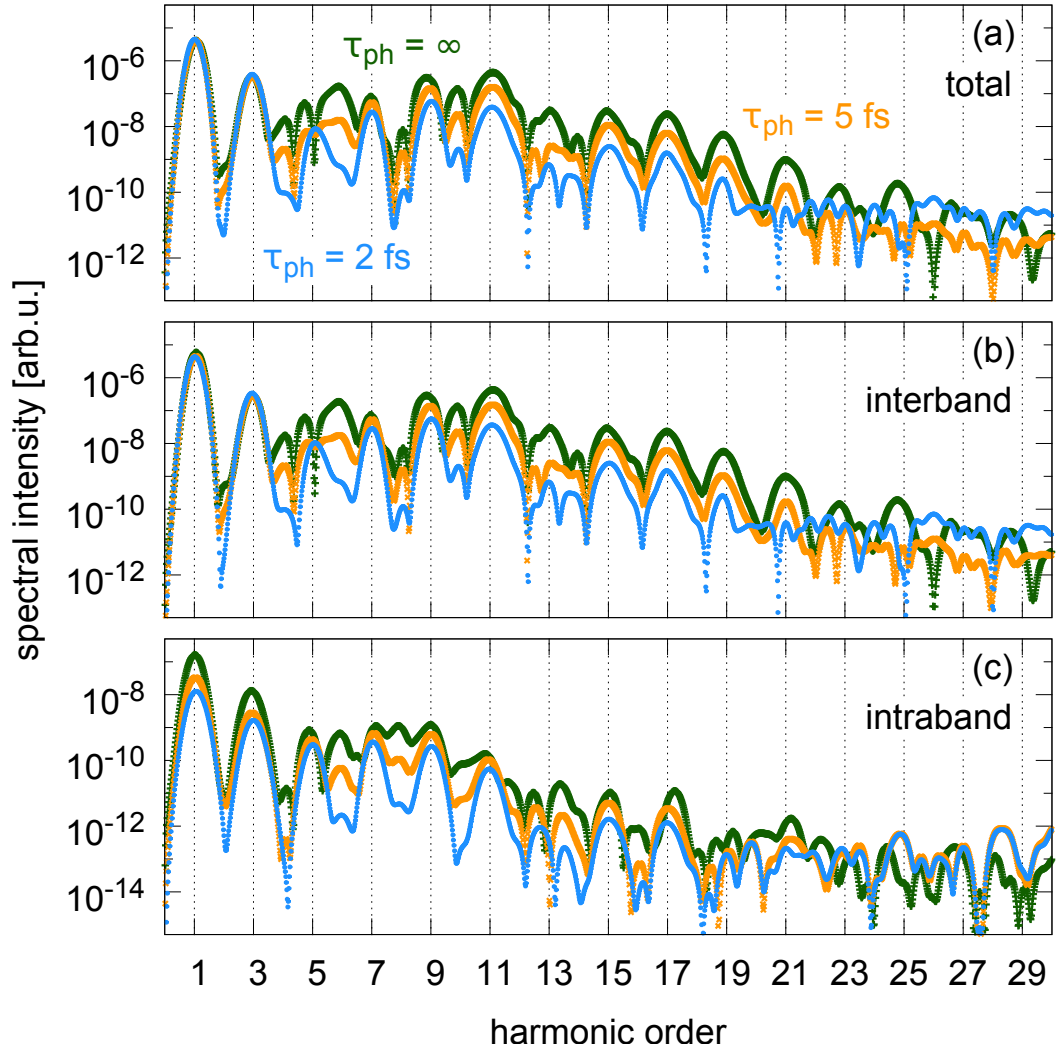


Figure 13: Total (a), interband (b), and intraband (c) HHG spectra induced by the laser pulse given in Fig. 12a for phenomenological damping times of  $\tau_{\text{ph}} = \infty$  (green),  $\tau_{\text{ph}} = 5$  fs (orange), and  $\tau_{\text{ph}} = 2$  fs (blue). For the Fourier transform of the current, we use a Gaussian window function with a width of  $\sigma_t = 2$  fs centered around  $\tau_0 = 15$  fs.

### 3.2.2 Drude friction

Another way of introducing phenomenological damping via a unitary description for friction was proposed by Neuhauser and Lopata [13]. Here, excitation energy is dissipated by adding a friction term to the Hamiltonian that couples the induced current density to a friction field. Within our TDDFT approach, this leads to numerical issues and gives unphysical features in the induced current density. Nevertheless, a similar method according to the classical Drude model and including an additional Drude friction field  $\mathbf{A}_{\text{friction}}(t) \propto -c \int_{t_0}^t dt' \mathbf{J}(t')$  in the KS Hamiltonian results in a reduction of the excitation energy of the system as well as in an exponential decay of the constant offset observed for the induced current in our linear response calculations (Sec. 2.2.2). Details are provided in [14].

## 3.3 Decoherence

Compared to HHG in single atoms the ionized part of the wave packet may scatter elastically off phonons or other electrons and, as a consequence, lose coherence with its parent wave packet. In conventional TDDFT, such processes are not accounted for and, therefore, the KS states remain fully coherent until the end of the simulation. In experiment, decoherence times as short as  $\tau_{\text{dec}} \leq 1$  fs have been reported [15] rendering these processes important interaction channels for any laser-solid simulation. A theoretical description, numerical implementation, and first applications of decoherence are presented in the following.

### 3.3.1 Theoretical description

We demonstrate the method for an electronic two level system  $\{|a\rangle, |b\rangle\}$ . Each electronic level has an additional degree of freedom  $|s\rangle$  given by the history of interaction with an external bath, for the time being, assumed to be a phonon bath. Here,  $|s\rangle = |0\rangle$  denotes the state that has not yet interacted with the bath, i.e., the electron has not been scattered by a phonon so far. Allowing only for energy and momentum

conserving scattering processes (changes in momentum by electron-phonon scattering are too small to be representable on our  $\mathbf{k}$ -grid) we get  $|a, s_i\rangle \rightarrow |a, s_j \neq s_i\rangle$  and  $|b, s_i\rangle \rightarrow |b, s_j \neq s_i\rangle$ , respectively. The initial state

$$|\psi_0\rangle = \alpha|a, 0\rangle + \beta|b, 0\rangle \quad (29)$$

with  $|\alpha|^2 + |\beta|^2 = 1$  is a coherent superposition of both electronic levels neither of which has so far been scattered. The electronic one-particle density matrix for this state is given by the trace over the additional degree of freedom  $|s\rangle$

$$\rho_0 = \text{Tr}_s |\psi_0\rangle\langle\psi_0| \Rightarrow \rho_0^{\{|a\rangle, |b\rangle\}} = \begin{pmatrix} |\alpha|^2 & \alpha\beta^* \\ \alpha^*\beta & |\beta|^2 \end{pmatrix}. \quad (30)$$

Note that for Eq. (29) as input Eq. (30) still represents a pure state. Later associating  $|a\rangle$  and  $|b\rangle$  with valence and conduction band states we assume that only  $|b\rangle$  couples to the external bath, i.e., has a non-vanishing probability to interact with phonons ( $\langle b, s_i | V_c | b, s_j \rangle \neq 0$  and  $\langle a, s_i | V_c | a, s_j \rangle = 0$  with the coupling potential  $V_c$  and  $s_i \neq s_j$ ). We find for  $|\psi\rangle$  after a small time step  $\Delta t$  to first order approximation in  $V_c$

$$|\psi(\Delta t)\rangle = \alpha|a, 0\rangle + \beta N(\Delta t)|b, 0\rangle + \beta N(\Delta t) \sum_{s>0} c_s(\Delta t)|b, s\rangle \quad (31)$$

with

$$N(\Delta t) = \frac{1}{\sqrt{1 + \sum_{s>0} |c_s(\Delta t)|^2}} \quad (32)$$

and

$$c_s(\Delta t) = -i\Delta t \langle b, s | V_c | b, 0 \rangle. \quad (33)$$

Note that for a particle in  $|b\rangle$  the scattering probability (i.e., the probability of interacting with the external bath) within the time interval  $\Delta t$  is given by  $1 - [N(\Delta t)]^2$ .

Calculating the density matrix

$$\rho(\Delta t)^{\{|a\rangle,|b\rangle\}} = \begin{pmatrix} |\alpha|^2 & \alpha\beta^*N(\Delta t) \\ \alpha^*\beta N(\Delta t) & |\beta|^2 \end{pmatrix} \quad (34)$$

we see that the off-diagonal elements are reduced indicating a loss of coherence, i.e., Eq. (34) no longer represents a pure but a mixed state. In the absence of external forces the system approaches the fully incoherent limit

$$\rho(t \rightarrow \infty)^{\{|a\rangle,|b\rangle\}} = \begin{pmatrix} |\alpha|^2 & 0 \\ 0 & |\beta|^2 \end{pmatrix}. \quad (35)$$

We now generalize the wave function (29) to an electronic  $N$  level system  $\{|a_1\rangle, \dots, |a_{N_a}\rangle, |b_1\rangle, \dots, |b_{N_b}\rangle\}$  with  $N_a$  valence band states and  $N_b$  conduction band states,  $N_a + N_b = N$ . Again, states  $|b_i\rangle$  couple to the external bath whereas states  $|a_i\rangle$  do not. Starting from the initial state

$$|\psi_0\rangle = \sum_{i=1}^{N_a} \alpha_i |a_i, 0\rangle + \sum_{i=1}^{N_b} \beta_i |b_i, 0\rangle \quad (36)$$

or, equivalently, the density matrix

$$\rho_0^{\{|a_i\rangle,|b_i\rangle\}} = \begin{pmatrix} \begin{array}{cccc|ccc} |\alpha_1|^2 & \alpha_1\alpha_2^* & \cdots & \alpha_1\alpha_{N_a}^* & \alpha_1\beta_1^* & \cdots & \alpha_1\beta_{N_b}^* \\ \alpha_1^*\alpha_2 & |\alpha_2|^2 & \cdots & \alpha_2\alpha_{N_a}^* & \alpha_2\beta_1^* & \cdots & \alpha_2\beta_{N_b}^* \\ \vdots & \vdots & \ddots & \vdots & \vdots & & \vdots \\ \alpha_1^*\alpha_{N_a} & \alpha_2^*\alpha_{N_a} & \cdots & |\alpha_{N_a}|^2 & \alpha_{N_a}\beta_1^* & \cdots & \alpha_{N_a}\beta_{N_b}^* \end{array} & \begin{array}{ccc} \alpha_1\beta_1^* & \cdots & \alpha_1\beta_{N_b}^* \\ \alpha_2\beta_1^* & \cdots & \alpha_2\beta_{N_b}^* \\ \vdots & & \vdots \\ \alpha_{N_a}\beta_1^* & \cdots & \alpha_{N_a}\beta_{N_b}^* \end{array} \\ \begin{array}{cccc|ccc} \alpha_1^*\beta_1 & \alpha_2^*\beta_1 & \cdots & \alpha_{N_a}^*\beta_1 & |\beta_1|^2 & \cdots & \beta_1\beta_{N_b}^* \\ \vdots & \vdots & & \vdots & \vdots & \ddots & \vdots \\ \alpha_1^*\beta_{N_b} & \alpha_2^*\beta_{N_b} & \cdots & \alpha_{N_a}^*\beta_{N_b} & \beta_1^*\beta_{N_b} & \cdots & |\beta_{N_b}|^2 \end{array} \end{pmatrix} \quad (37)$$

with  $\sum_{i=1}^{N_a} |\alpha_i|^2 + \sum_{i=1}^{N_b} |\beta_i|^2 = 1$  and using the scattering probability  $1 - [N_{b_i}(\Delta t)]^2$  for a particle in  $|b_i\rangle$ , we find that within the time interval  $\Delta t$  coherences (i.e., off-diagonal elements in the density matrix) between valence and conduction band states  $|a_i\rangle$  and  $|b_j\rangle$  (blue regions in Eq. (37)) are reduced by a factor  $N_{b_j}(\Delta t)$ . Coherences between  $|b_i\rangle$  and  $|b_j\rangle$  within the conduction band (red regions in Eq. (37)) are reduced by a factor  $N_{b_i}(\Delta t)N_{b_j}(\Delta t)$  and, therefore, damped more strongly than coherences between valence and conduction band states. Due to the vanishing scattering probability of  $|a_i\rangle$ , coherences between  $|a_i\rangle$  and  $|a_j\rangle$  within the valence band (green regions in Eq. (37)) are not affected.

### 3.3.2 Numerical implementation in TDDFT

For the time being we only treat scattering processes that do not change the electronic part of the wavefunction, i.e.,  $\mathbf{k}$ -changing processes are neglected. Therefore, the algorithm presented in this section is performed individually at each  $\mathbf{k}$ -point (to simplify the notation,  $\mathbf{k}$ -indices are omitted). For simplicity, all conduction band states have the same scattering probability in the following indicating an energy/momentum independent scattering probability for all conduction band states.

In order to include decoherence in the TDDFT code, it is necessary to propagate  $N^b > N^{\text{vb}}$  orbitals where  $N^{\text{vb}}$  denotes the number of the initially occupied valence bands. We start from the GS orbitals

$$|\psi_n(t=0)\rangle = |\psi_n^{\text{GS}}\rangle \quad n = 1, \dots, N^b \quad (38)$$

with the GS occupation numbers

$$N_n = \begin{cases} \text{const.} & n = 1, \dots, N^{\text{vb}} \\ 0 & n = N^{\text{vb}} + 1, \dots, N^b. \end{cases} \quad (39)$$

In addition to the conventional time propagation (4) we expand the time dependent

KS orbitals at every few time steps

$$\sqrt{N_n}|\psi_n\rangle = \sum_{m=1}^{N^b} c_{mn}|\psi_m^H\rangle + |h_n\rangle \quad (40)$$

into Houston basis functions  $|\psi_n^H\rangle$  by computing the coefficients

$$c_{mn} = \sqrt{N_n}\langle\psi_m^H|\psi_n\rangle. \quad (41)$$

Since our Houston basis  $\{|\psi_1^H\rangle, \dots, |\psi_{N^b}^H\rangle\}$  is not complete, we collect the remainder (which, for a sufficiently large number of bands  $N^b$ , is a tiny contribution to the KS orbitals  $\langle h_n|h_n\rangle \lll 1$  as shown in convergence studies involving an increasing number of CB states) in *helper* wavefunctions defined by

$$|h_n\rangle = \sqrt{N_n}|\psi_n\rangle - \sum_{m=1}^{N^b} c_{mn}|\psi_m^H\rangle. \quad (42)$$

With this we get the sum of all one-particle density matrices weighted with their occupation numbers  $\rho_{\text{tot}} = \sum_{n=1}^{N^b} N_n|\psi_n\rangle\langle\psi_n|$  (in the Houston basis and without *helper* contributions)

$$\rho_{\text{tot}}^{\{H\}} = \begin{pmatrix} \rho_{11} & \rho_{12} & \cdots & \rho_{1N^b} \\ \rho_{21} & \rho_{22} & \cdots & \rho_{2N^b} \\ \vdots & \vdots & \ddots & \vdots \\ \rho_{N^b1} & \rho_{N^b2} & \cdots & \rho_{N^bN^b} \end{pmatrix} = \sum_{n=1}^{N^b} \begin{pmatrix} |c_{1n}|^2 & c_{1n}c_{2n}^* & \cdots & c_{1n}c_{N^bn}^* \\ c_{2n}c_{1n}^* & |c_{2n}|^2 & \cdots & c_{2n}c_{N^bn}^* \\ \vdots & \vdots & \ddots & \vdots \\ c_{N^bn}c_{1n}^* & c_{N^bn}c_{2n}^* & \cdots & |c_{N^bn}|^2 \end{pmatrix} \quad (43)$$

which allows us to incorporate decoherence by reducing the red and blue marked off-

diagonal elements

$$\rho_{\text{tot}}^{\{\text{H}\}} = \begin{pmatrix} \begin{array}{cccc|ccc} \rho_{11} & \rho_{12} & \cdots & \rho_{1N^{\text{vb}}} & \rho_{1N^{\text{vb}}+1} & \cdots & \rho_{1N^{\text{b}}} \\ \rho_{21} & \rho_{22} & \cdots & \rho_{2N^{\text{vb}}} & \rho_{2N^{\text{vb}}+1} & \cdots & \rho_{2N^{\text{b}}} \\ \vdots & \vdots & \ddots & \vdots & \vdots & & \vdots \\ \rho_{N^{\text{vb}}1} & \rho_{N^{\text{vb}}2} & \cdots & \rho_{N^{\text{vb}}N^{\text{vb}}} & \rho_{N^{\text{vb}}N^{\text{vb}}+1} & \cdots & \rho_{N^{\text{vb}}N^{\text{b}}} \end{array} & \begin{array}{ccc} \rho_{1N^{\text{vb}}+1} & \cdots & \rho_{1N^{\text{b}}} \\ \rho_{2N^{\text{vb}}+1} & \cdots & \rho_{2N^{\text{b}}} \\ \vdots & & \vdots \\ \rho_{N^{\text{vb}}N^{\text{vb}}+1} & \cdots & \rho_{N^{\text{vb}}N^{\text{b}}} \end{array} \\ \begin{array}{cccc|ccc} \rho_{N^{\text{vb}}+11} & \rho_{N^{\text{vb}}+12} & \cdots & \rho_{N^{\text{vb}}+1N^{\text{vb}}} & \rho_{N^{\text{vb}}+1N^{\text{vb}}+1} & \cdots & \rho_{N^{\text{vb}}+1N^{\text{b}}} \\ \vdots & \vdots & & \vdots & \vdots & \ddots & \vdots \\ \rho_{N^{\text{b}}1} & \rho_{N^{\text{b}}2} & \cdots & \rho_{N^{\text{b}}N^{\text{vb}}} & \rho_{N^{\text{b}}N^{\text{vb}}+1} & \cdots & \rho_{N^{\text{b}}N^{\text{b}}} \end{array} & \begin{array}{ccc} \rho_{N^{\text{vb}}+1N^{\text{vb}}+1} & \cdots & \rho_{N^{\text{vb}}+1N^{\text{b}}} \\ \vdots & \ddots & \vdots \\ \rho_{N^{\text{b}}N^{\text{vb}}+1} & \cdots & \rho_{N^{\text{b}}N^{\text{b}}} \end{array} \end{pmatrix} \quad (44)$$

Applying the rules derived in Sec. 3.3.1, the white and green marked elements remain the same whereas the blue and red marked elements are multiplied with  $e^{-\Delta t/\tau_{\text{dec}}}$  and  $e^{-2\Delta t/\tau_{\text{dec}}}$ , respectively, with  $\tau_{\text{dec}} \simeq \frac{\Delta t}{1-N(\Delta t)}$  [Eq. (34)] being the decoherence time which depends on the scattering matrix elements. Note that allowing for energy/momentum dependent scattering probabilities leads to band- and  $\mathbf{k}$ -dependent decoherence times.

Finally, we determine new KS orbitals from the modified density matrix  $\tilde{\rho}_{\text{tot}}$  obtained after applying decoherence ( $\rho_{\text{tot}} \xrightarrow{\text{decoherence}} \tilde{\rho}_{\text{tot}}$ ). Of course, this decomposition is not unique. We have adapted the following procedure: we set the first KS state (not normalized and without *helper* contribution) to

$$|\tilde{\Phi}_1\rangle^{\{\text{H}\}} = \frac{1}{\sqrt{\tilde{\rho}_{11}}} \begin{pmatrix} \tilde{\rho}_{11} \\ \tilde{\rho}_{21} \\ \vdots \\ \tilde{\rho}_{N^{\text{b}}1} \end{pmatrix} \quad (45)$$

such that the remaining density matrix (without *helper* contributions)

$$\begin{aligned}
\tilde{\rho}_{R_1}^{\{H\}} &= \begin{pmatrix} \tilde{\rho}_{11} & \tilde{\rho}_{12} & \cdots & \tilde{\rho}_{1N^b} \\ \tilde{\rho}_{21} & \tilde{\rho}_{22} & \cdots & \tilde{\rho}_{2N^b} \\ \vdots & \vdots & \ddots & \vdots \\ \tilde{\rho}_{N^b1} & \tilde{\rho}_{N^b2} & \cdots & \tilde{\rho}_{N^bN^b} \end{pmatrix} - \frac{1}{\tilde{\rho}_{11}} \begin{pmatrix} \tilde{\rho}_{11} \\ \tilde{\rho}_{21} \\ \vdots \\ \tilde{\rho}_{N^b1} \end{pmatrix} \begin{pmatrix} \tilde{\rho}_{11}^* & \tilde{\rho}_{21}^* & \cdots & \tilde{\rho}_{N^b1}^* \end{pmatrix} \\
&= \begin{pmatrix} 0 & 0 & \cdots & 0 \\ 0 & \tilde{\rho}_{22} - \frac{\tilde{\rho}_{21}\tilde{\rho}_{12}}{\tilde{\rho}_{11}} & \cdots & \tilde{\rho}_{2N^b} - \frac{\tilde{\rho}_{21}\tilde{\rho}_{1N^b}}{\tilde{\rho}_{11}} \\ \vdots & \vdots & \ddots & \vdots \\ 0 & \tilde{\rho}_{N^b2} - \frac{\tilde{\rho}_{N^b1}\tilde{\rho}_{12}}{\tilde{\rho}_{11}} & \cdots & \tilde{\rho}_{N^bN^b} - \frac{\tilde{\rho}_{N^b1}\tilde{\rho}_{1N^b}}{\tilde{\rho}_{11}} \end{pmatrix}
\end{aligned} \tag{46}$$

has no contributions of the energetically lowest Houston state  $|\psi_1^H\rangle$ . In the next step,  $|\tilde{\Phi}_2\rangle$  is chosen in such a way that the remaining part of the density matrix  $\tilde{\rho}_{R_2}^{\{H\}}$  has no contributions of the lowest two Houston states  $|\psi_1^H\rangle$  and  $|\psi_2^H\rangle$ , and so on. In order to conserve the number of particles as accurately as possible, we finally add the *helper* wavefunctions  $|\tilde{h}_n\rangle$ <sup>8</sup> to get the new KS orbitals

$$\sqrt{\tilde{N}_n}|\tilde{\psi}_n\rangle = |\tilde{\Phi}_n\rangle + |\tilde{h}_n\rangle. \tag{47}$$

### 3.3.3 First applications

First investigations of decoherence in the test system diamond provide very interesting results. In contrast to phenomenological damping (Sec. 3.2.1), decoherence increases the number of excited carriers and, therefore, the excitation energy of the system (Fig. 14). Both methods show enhanced hole densities in the VB for very similar reasons: while in the case of phenomenological damping CB electrons are removed

<sup>8</sup>Note that the *helper* wavefunctions are added as accurately as possible. E.g., when calculating  $|h_1\rangle$  according to Eq. (42) we determine the largest Houston contribution of  $|\psi_1\rangle$ , i.e., we find  $i$  such that  $|c_{i1}| \geq |c_{j1}|$  for  $1 \leq j \leq N^b$ . Consequently,  $|\tilde{h}_i\rangle = e^{i\phi_1}|h_1\rangle$  where  $\phi_1$  ensures that the relative phase between  $c_{i1}|\psi_i^H\rangle$  and  $|h_1\rangle$  given in  $|\psi_1\rangle$  is conserved. Therefore, in general  $|h_1\rangle \neq |\tilde{h}_1\rangle$ . Furthermore, when repeating this procedure for all other KS orbitals  $|\psi_k\rangle$  with  $k > 1$ , the coefficients of the  $i^{\text{th}}$  Houston state  $c_{ik}$  are excluded from consideration. This means that each KS state  $|\tilde{\psi}_n\rangle$  gets exactly one *helper* wavefunction  $|\tilde{h}_n\rangle$ .

before they return into the VB, decoherence reduces the probability for recombination of the excited part of the wave function into the hole left in the VB. Since the particle number is conserved here, decoherence enforces increased VB hole and CB electron densities.

This explains the observed effect of decoherence on the induced current densities (Fig. 15): more electrons in the CB increase the CB (i.e., intraband) current (Fig. 15d). Similarly, more holes in the VB increase the VB current which adds to the interband signal for our decomposition of currents. Due to its phase shift by  $\pi$  relative to the *real* interband current, the increased hole current results in a reduction and phase shift of  $\mathbf{J}^{\text{er}}(t)$  in our calculations (Fig. 15c). The increase of conduction band and hole currents with shorter decoherence times finally leads to a phase-shift of the total current by almost  $\pi$  (Fig. 15b).

Extensive studies on the optical Bloch equations (OBEs) and the influence of short dephasing times  $T_2$  [1] have shown similar effects on the HHG spectrum as observed in our simulations accounting for decoherence in TDDFT. Decreasing decoherence times  $\tau_{\text{dec}}$  in TDDFT reproduce the main modifications observed for short  $T_2$ : while, in general, the intensities of the lowest harmonics increase<sup>9</sup>, the intensities of the highest harmonics are reduced for shorter  $\tau_{\text{dec}}$  or  $T_2$  indicating that the highest harmonics mainly originate from interband coherences. In the “middle” part of the spectrum, frequencies between the odd harmonics are damped out efficiently leading to a more pronounced harmonic structure (Figs. 16, 17). As different Fourier components of the scanned dispersion relations uniquely contribute to the intraband spectrum [2], special features of the band structure also strongly influence the interband spectrum. Therefore, the relative change of individual harmonics as function of  $\tau_{\text{dec}}$  and laser-pulse intensity sensitively depends on the shape of the band structure opening the pathway to an all-optical determination of crystal band structures.

---

<sup>9</sup>Due to the phase shift of  $\pi$  between inter- and intraband currents the intensity of the first harmonic at first decreases and finally increases with decreasing  $\tau_{\text{dec}}$ .

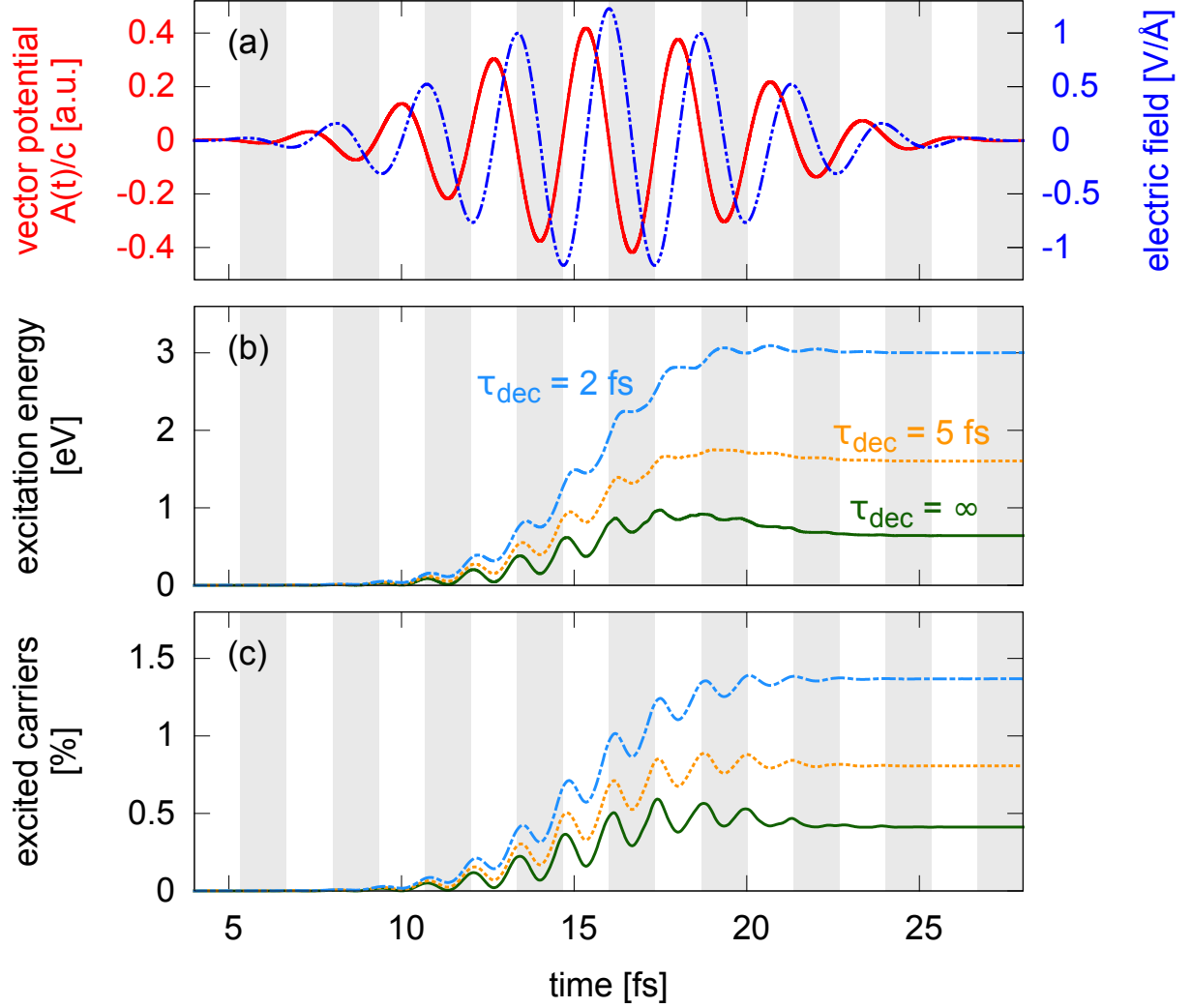


Figure 14: (a) Electric field with a  $\cos^6$ -envelope, peak intensity  $I_{\max} = 2 \times 10^{13} \text{ W/cm}^2$ ,  $\hbar\omega_L = 1.55 \text{ eV}$ , and  $\phi_{\text{CE}} = 0$  (blue), and the corresponding input vector potential  $\mathbf{A}(t)/c$  (red) (same pulse as in Sec. 2.2.1). (b-c) Excitation energy within one unit cell (including 4 carbon atoms) (b), and percentage of conduction band electrons (c) as functions of time. Green, orange, and blue curves correspond to decoherence times of  $\tau_{\text{dec}} = \infty$ ,  $\tau_{\text{dec}} = 5 \text{ fs}$ , and  $\tau_{\text{dec}} = 2 \text{ fs}$ .

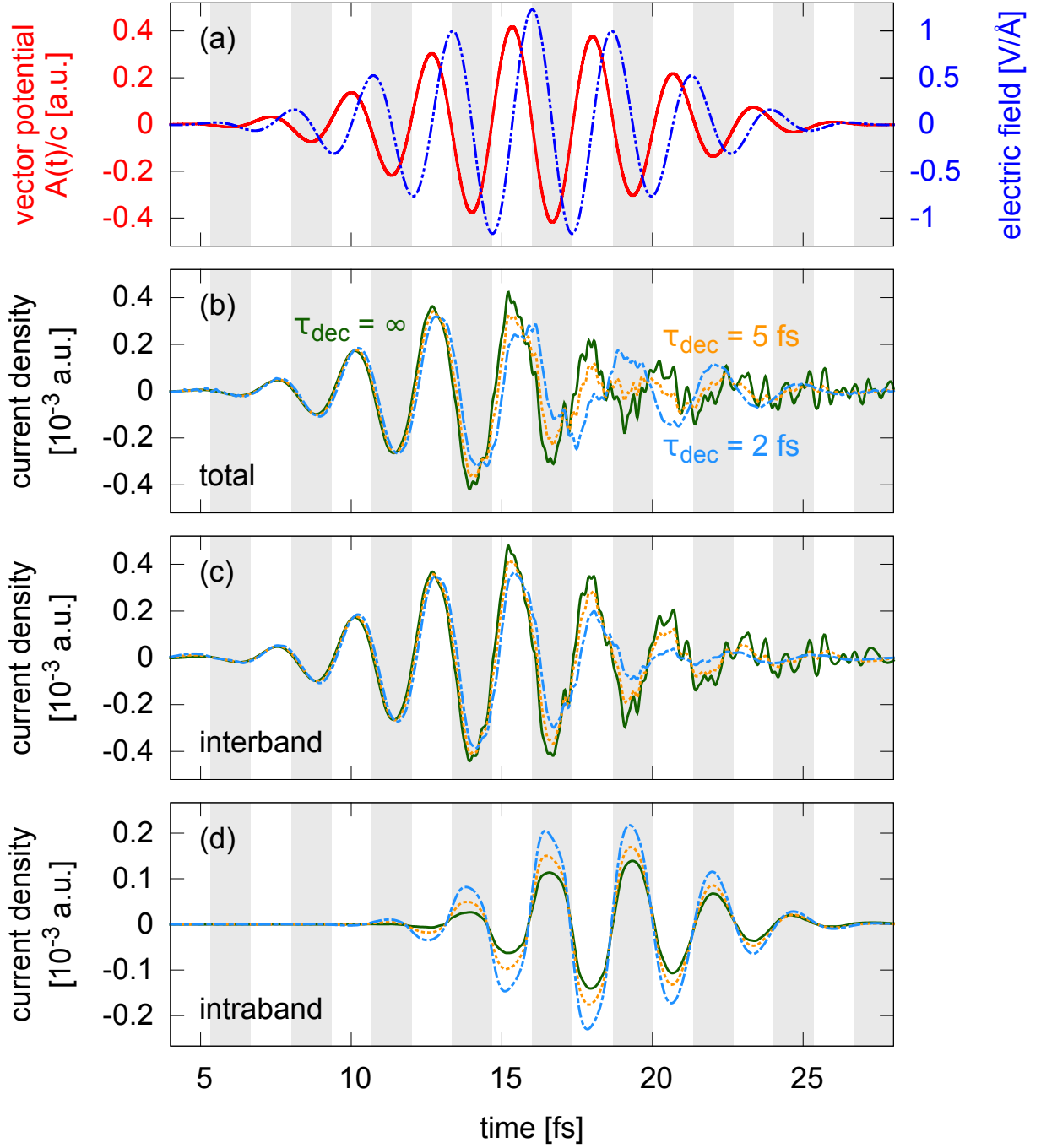


Figure 15: (a) Same as in Fig. 14a. (b-d) Induced total (b), interband (c), and intraband (d) current densities along the laser polarization direction as functions of time. Green, orange, and blue curves correspond to decoherence times of  $\tau_{\text{dec}} = \infty$  (green),  $\tau_{\text{dec}} = 5$  fs (orange), and  $\tau_{\text{dec}} = 2$  fs (blue).

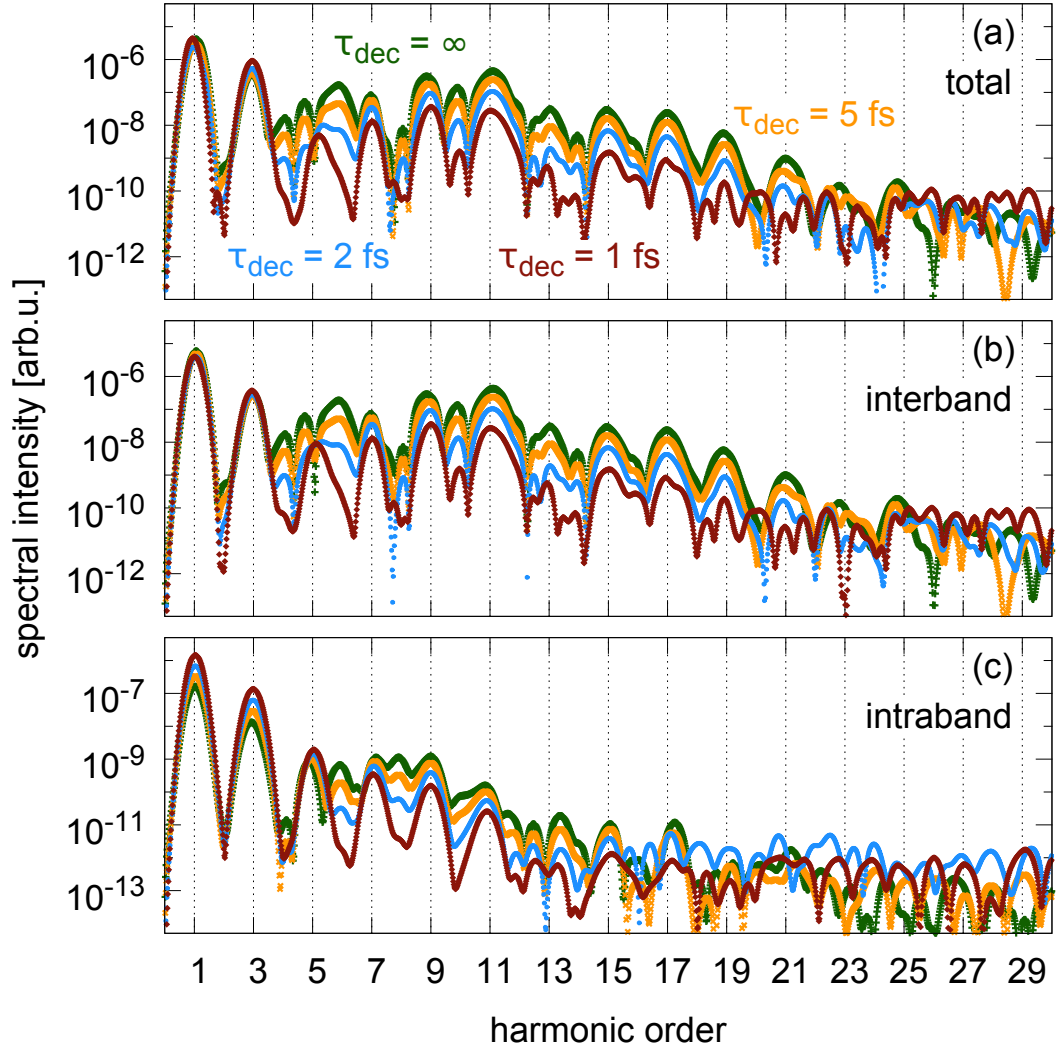


Figure 16: Total (a), interband (b), and intraband (c) HHG spectra induced by the laser pulse given in Fig. 15a for decoherence times of  $\tau_{\text{dec}} = \infty$  (green),  $\tau_{\text{dec}} = 5$  fs (orange),  $\tau_{\text{dec}} = 2$  fs (blue), and  $\tau_{\text{dec}} = 1$  fs (brown). For the Fourier transform of the current, we use a Gaussian window function with a width of  $\sigma_t = 2$  fs centered around  $\tau_0 = 15$  fs.

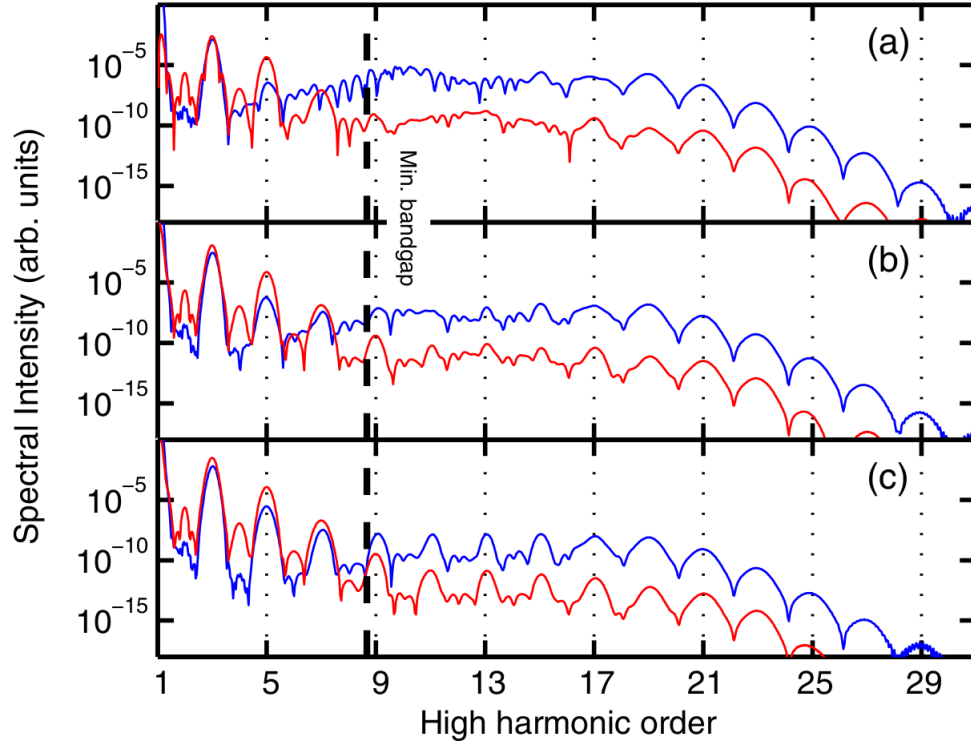


Figure 17: Simulated interband (blue) and intraband (red) spectra from OBE calculations for  $T_2 = \infty$  (a), 5.4 fs (b), and 2.7 fs (c) induced by a 10 cycle pulse with carrier frequency  $\hbar\omega_L = 0.38$  eV (3270 nm; figure reproduced from [1]). In this work, the intraband current consists of both CB and hole currents. Still, interband HHG above the band-gap energy dominates at high frequencies by orders of magnitude.

### 3.3.4 Numerical details

The major problem of the current implementation is the  $\mathbf{k}$ -discretization of the Houston grid. Ideally, the set of basis functions chosen for the expansion (40) of the KS orbitals is defined by the effective vector potential providing a shift (8) in reciprocal space. For the calculations in Sec. 3.3.3 we use a refined Houston grid of  $\Delta k^{\text{H}} \simeq 0.004$  a.u. ( $\Delta k \simeq 0.06$  a.u.) including  $N^{\text{b}} = 28$  orbitals ( $N^{\text{vb}} = 8$ ). Every 5 time steps<sup>10</sup> ( $\Delta t_{\text{dec}} = 0.1$  a.u.) a decoherence sequence is applied where the closest point of the refined grid defines the basis for the projection. To ensure smooth transitions between Houston expansions for neighboring grid points, a rather fine Houston grid is necessary. Long time intervals between these jumps affect the numerical stability (Fig. 18). The required refined  $\mathbf{k}$ -grid spacing strongly decreases with decreasing pulse intensity, photon energy, and decoherence time. Especially for numerically more demanding systems ( $\text{SiO}_2$ ,  $\text{ZnSe}$ , ...) the number of available Houston grid points is limited by the available memory (on VSC3). Therefore, the first step for future investigations aims at implementing an interpolation procedure between neighboring Houston basis functions.

---

<sup>10</sup>Carefully choosing all the simulation parameters guarantees converged results. Note that constant time steps  $\Delta t_{\text{dec}}$  between decoherence occurrences are very important for numerical stability.

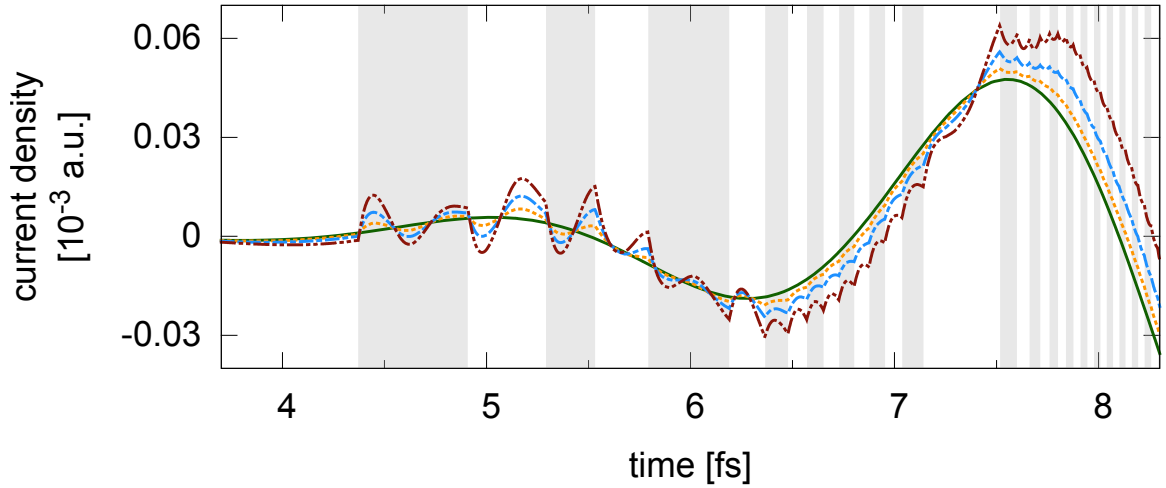


Figure 18: Magnification of Fig. 15b: induced total current densities as functions of time for  $\tau_{\text{dec}} = \infty$  (green),  $\tau_{\text{dec}} = 5$  fs (orange),  $\tau_{\text{dec}} = 2$  fs (blue), and  $\tau_{\text{dec}} = 1$  fs (brown). The boundaries between white and shaded regions indicate jumps between neighboring Houston grid points.

### 3.3.5 Conclusions and outlook

We have developed a method to include decoherence in TDDFT showing very promising preliminary results. In the current implementation all conduction band states dephase within the time  $\tau_{\text{dec}}$  given as an external parameter of the simulation. Still, the real numerical value and energy- or  $\mathbf{k}$ -dependence of  $\tau_{\text{dec}}$  are to be determined. Furthermore, the identification of the dominantly contributing physical process (electron-electron vs. electron-phonon scattering) is subject of ongoing investigations. Therefore, we will determine the corresponding scattering matrix elements.

## 4 HHG from $\alpha$ -quartz irradiated by transients

### 4.1 Motivation

Recently, Luu et al. have reported on HHG from thin films ( $\sim 125$  nm) of polycrystalline  $\text{SiO}_2$  irradiated by strong and short (few-cycle down to sub-cycle) laser pulses [2]. The pulses were characterized via attosecond streaking, the radiation emitted from the sample was recorded after transmission through an Al filter cutting frequencies below 15 eV (Fig. 19).

Luu et al. interpret the data based on a solution of the optical Bloch equations in 1D (along the high symmetry lines  $\Gamma K$ ,  $\Gamma M$ , or  $\Gamma A$  (see Fig. 22)) for the lowest conduction and uppermost valence bands. They conclude that intraband harmonics from the conduction band and induced by laser pulses polarized parallel to  $\Gamma M$  dominantly contribute to the emitted radiation from the polycrystalline target. The intensity of individual harmonics would depend on details of the electronic structure allowing for an all-optical reconstruction of the dispersion relation of the conduction band. Contributions of interband HHG would be insignificant. In the following we test this interpretation of the measured HHG spectra using our TDDFT simulations.

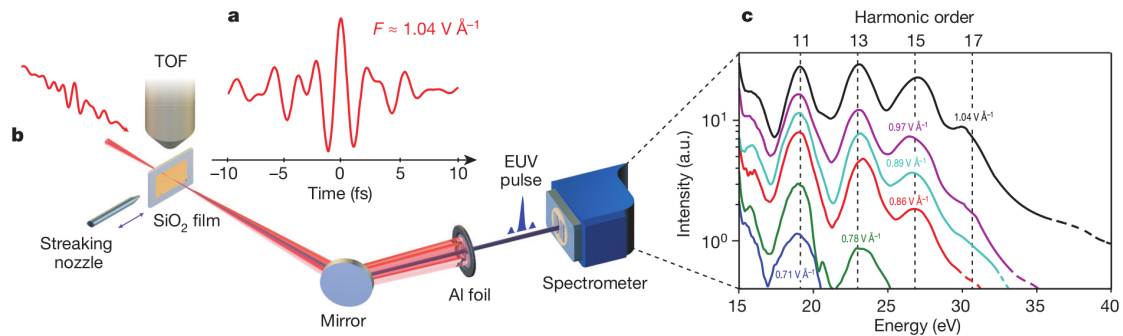


Figure 19: Input pulse (a), experimental setup (b), and measured HHG spectra (c) for various pulse intensities used by Luu et al. (figure taken from [2]).

## 4.2 Simulation results

### 4.2.1 Simulated crystal

Being restricted to Cartesian grids, we use a cuboid  $a \times b \times c = 9.28 \times 16.05 \times 10.21$  a.u.<sup>3</sup> unit cell (Figs. 20, 21) including 12 oxygen and 6 silicon atoms [16].  $O[1s^2]$  and  $Si[1s^2 2s^2 2p^6]$  electrons are frozen in norm-conserving pseudopotentials leaving 48 doubly occupied KS orbitals to propagate with a time step of  $\Delta t = 0.02$  a.u. The Cartesian grids in real and reciprocal space parallel (orthogonal) to the polarization direction have step sizes of  $\Delta x \simeq 0.3$  (0.4) a.u. and  $\Delta k \simeq 0.04$  (0.08) a.u., respectively. Applying the TBmBJ functional with  $c = 1$  [17], good agreement between measured and calculated dielectric functions is found [16].  $\alpha$ -quartz shows broken inversion symmetry along the  $\hat{a}$ -direction leading to, e.g., the generation of odd and even harmonics for laser polarizations parallel to  $\hat{a}$ . For all directions ( $\Gamma K \parallel \hat{a}$ ,  $\Gamma M \parallel \hat{b}$ ,  $\Gamma A \parallel \hat{c}$ ) the energetically highest valence band is rather flat compared to the lowest conduction band (Fig. 22).

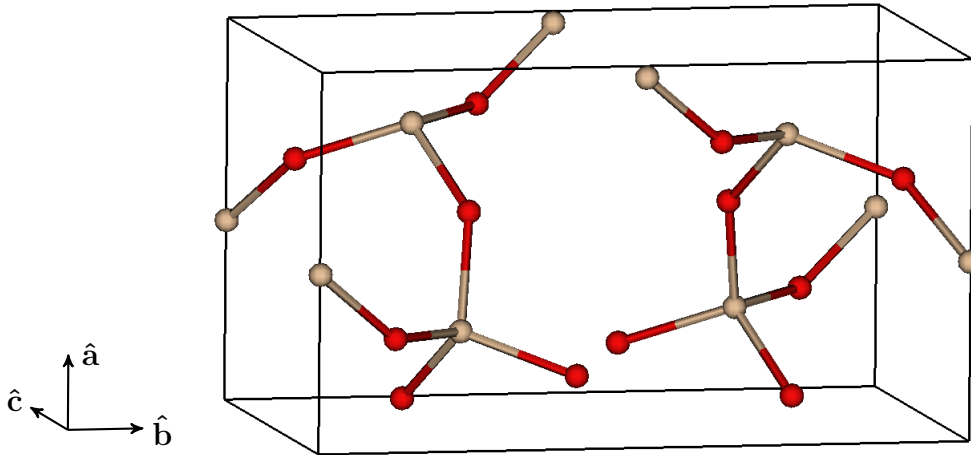
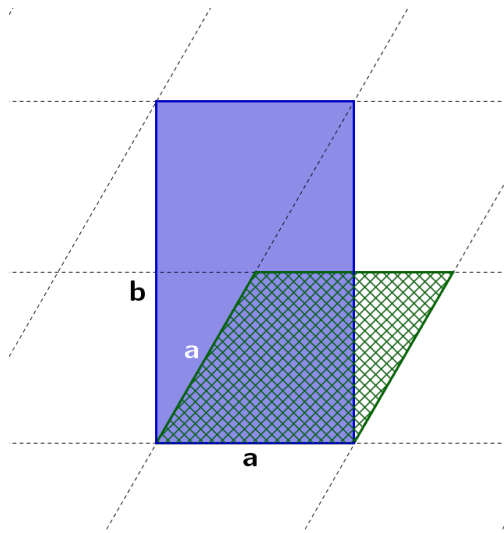
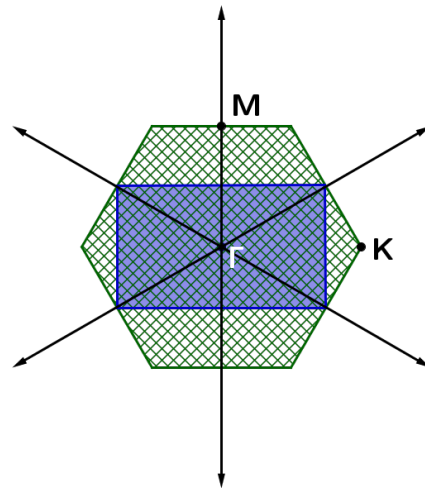


Figure 20: Unit cell of  $\alpha$ -quartz containing 12 oxygen (red) and 6 silicon (beige) atoms and their periodic replicas on the unit cell boundary.



(a) Real space.



(b) Reciprocal space.

Figure 21: Cut of the primitive (green) and cuboid (blue) unit cell of  $\alpha$ -quartz orthogonal to the  $\hat{c}$ -axis in real (a) and reciprocal (b) space.

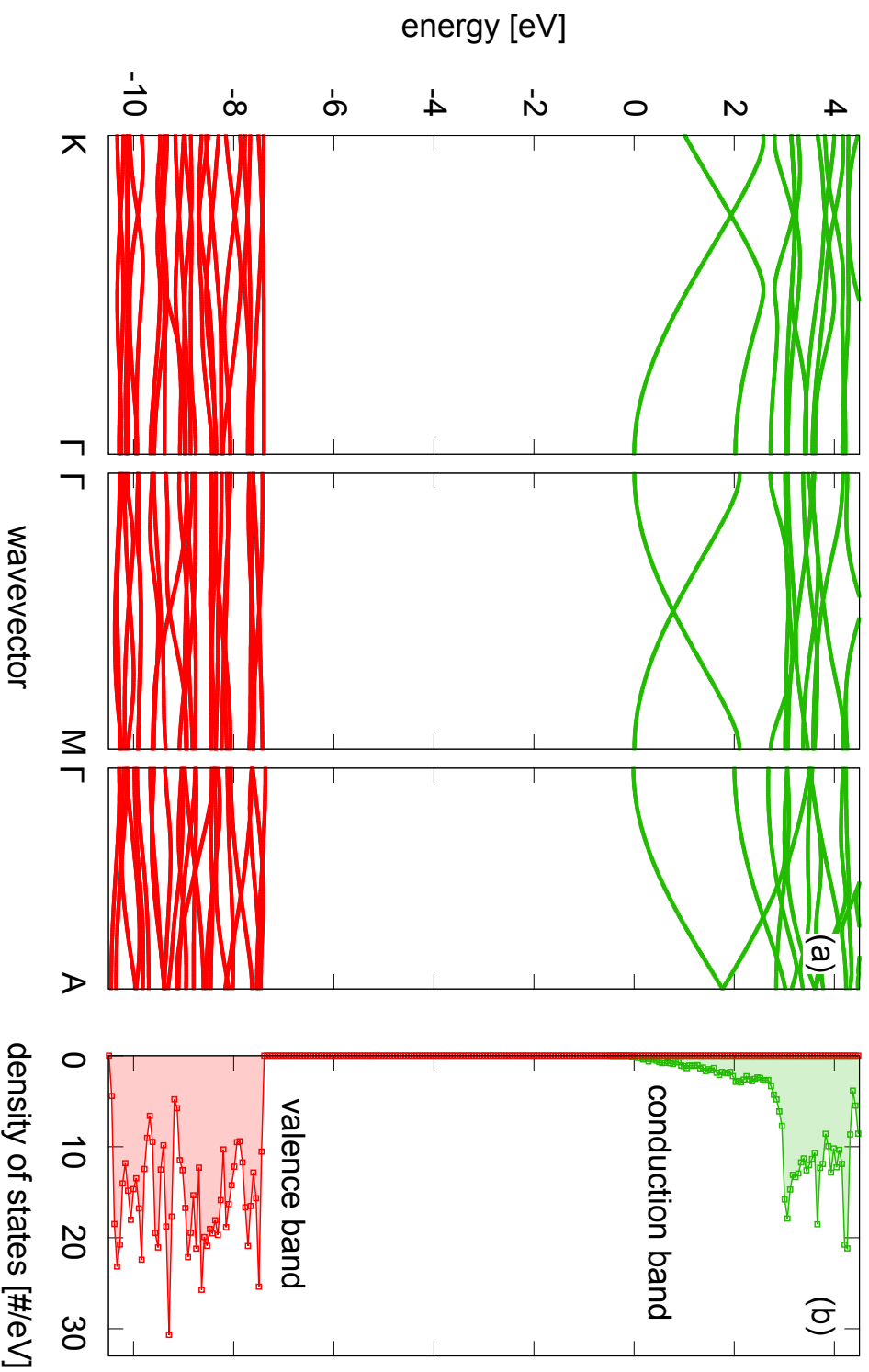


Figure 22: Simulated valence (red) and conduction (green) band structure (a) and density of states (b) of the  $\text{SiO}_2$  crystal. Due to the Cartesian  $\mathbf{k}$ -point grid arranged symmetrically with respect to but not containing  $\Gamma$  (cf. Fig. 1a), the dispersion relations shown correspond to lines slightly displaced (by  $\Delta k \simeq 0.03$  a.u.) parallel to the high symmetry lines.

### 4.2.2 Transients on $\alpha$ -quartz

For this simulation we fit the central region of the transients (i.e. very short pulses) used in the experiment by

$$\mathbf{E}(t) = \mathbf{E}_{\max} \cos^8\left(\frac{\omega_L}{12}t\right) \cos(\omega_L t + \phi_{\text{CE}}) \quad (48)$$

yielding  $\hbar\omega_L = 1.802\text{eV}$  and  $\phi_{\text{CE}} = -0.3$  (Fig. 23a). Starting from the fitted value for  $|\mathbf{E}_{\max}| = 1.07 \text{ V/\AA}$  ( $I_{\max} \simeq 1.5 \times 10^{13} \text{ W/cm}^2$ ), we gradually increase the peak field to  $|\mathbf{E}_{\max}| = 2.5 \text{ V/\AA}$  ( $I_{\max} \simeq 8.3 \times 10^{13} \text{ W/cm}^2$ ) in order to reproduce the measured energy cutoff.

Comparing three calculations for polarizations parallel to  $\Gamma K$ ,  $\Gamma M$ , and  $\Gamma A$  using the latter pulse (Eq. (48) with  $|\mathbf{E}_{\max}| = 2.5 \text{ V/\AA}$ ; see Fig. 23a) we find very similar results. In each case the induced total current density is dominated by its interband contribution. Before the pulse maximum the input vector potential and the induced currents are in phase indicating bound electron motion. Close to the pulse maximum when the probability for electron excitation to the conduction band is largest, pronounced non-linear contributions emerge. Furthermore, the enhanced excited carrier contribution leads to a phase shift in the current density after the field maximum (Fig. 23b).

According to the simple estimate from Sec. 2.2.1 (conduction band electrons behave like free particles), the vector potential and the induced intraband current should be phase-shifted by  $\pi$ . Here, however, the conduction band currents are shifted only by about  $\pi/2$  (Fig. 23c). This underlines the strong influence of the shape of the conduction band structure of  $\text{SiO}_2$  (containing regions of rather flat dispersion relations; see Fig. 22) on the induced intraband current density.

As expected from the relative intensities of total and intraband current densities, intraband HHG contributes only  $\lesssim 1\%$  to the total spectrum over the whole frequency range (Fig. 24). While the spectral ranges above the 5<sup>th</sup> harmonic for all polarization directions are very noisy their incoherent superposition gives especially for the intra-

band spectrum (Fig. 24b) a surprisingly clear harmonic structure indicating that a large fraction of the noise is generated by coherences between valence and conduction band states. Therefore, imposing decoherence is indispensable for future investigations.

Comparing the three polarization directions we find very similar spectra below the 5<sup>th</sup> harmonic (Figs. 24a, 25). The broad spectral range of the short pulse used here results in broad harmonics with overlapping neighboring odd harmonics. Therefore, the even harmonics usually observed for polarizations parallel to  $\Gamma K$  and for longer pulses with their narrow spectral bandwidth are in this calculation reduced to increased spectral intensities between the odd harmonics compared to the two orthogonal polarization directions (visible between 1<sup>st</sup> and 3<sup>rd</sup>, and 3<sup>rd</sup> and 5<sup>th</sup> harmonics in Figs. 24a, 25).

As already discussed for the induced current density, the strongest (1<sup>st</sup> order) contribution can be related to the motion of bound electrons. For all three polarization directions the maxima of the emitted radiation coincide with the extrema of the electric field (Fig. 26), since the induced currents are in phase with the input vector potential. The emission of radiation at higher frequencies (harmonics 11 to 17) sets in at the pulse maximum and has its maximum value shortly after the pulse maximum. In this high energy range the most intense contribution to the overall spectrum (i.e. incoherent superposition) is found for laser polarizations parallel to  $\Gamma A$  and, to a lesser extend, for  $\Gamma K$  (Fig. 26).

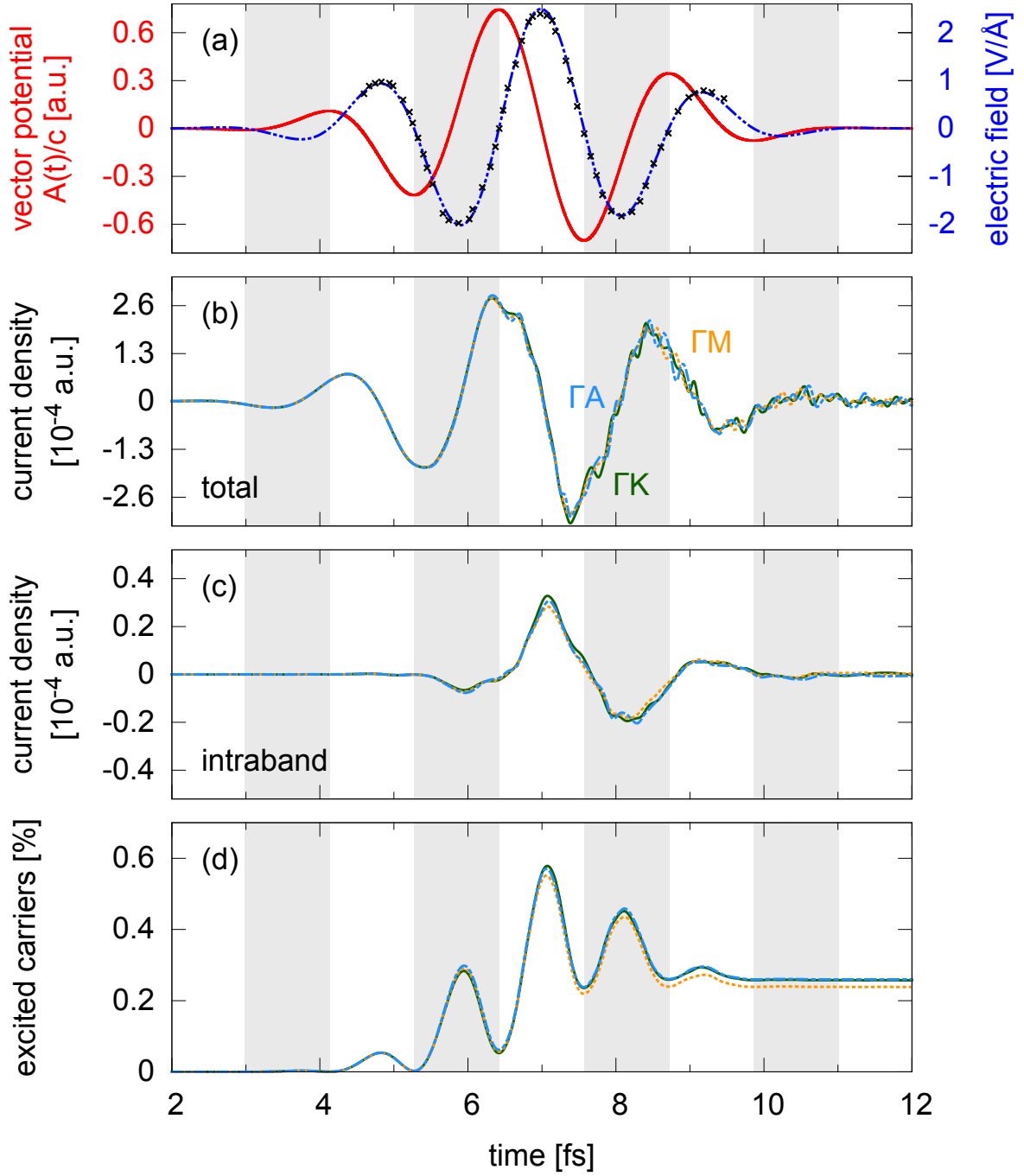


Figure 23: (a) Experimental pulse (scaled in amplitude) within the central region (black crosses, Fig. 19a), the fitted electric field (48) with a  $\cos^8$ -envelope, peak intensity of  $I_{\max} \simeq 8.3 \times 10^{13} \text{ W/cm}^2$ ,  $\hbar\omega_L = 1.802 \text{ eV}$ , and  $\phi_{\text{CE}} = -0.3$  (blue line), and the corresponding input vector potential  $\mathbf{A}(t)/c$  (red line). (b-d) Induced total (b) and intraband (c) current densities, and the occupation of conduction band states (d) for laser polarizations parallel to  $\Gamma K$  (green),  $\Gamma M$  (orange), and  $\Gamma A$  (blue).

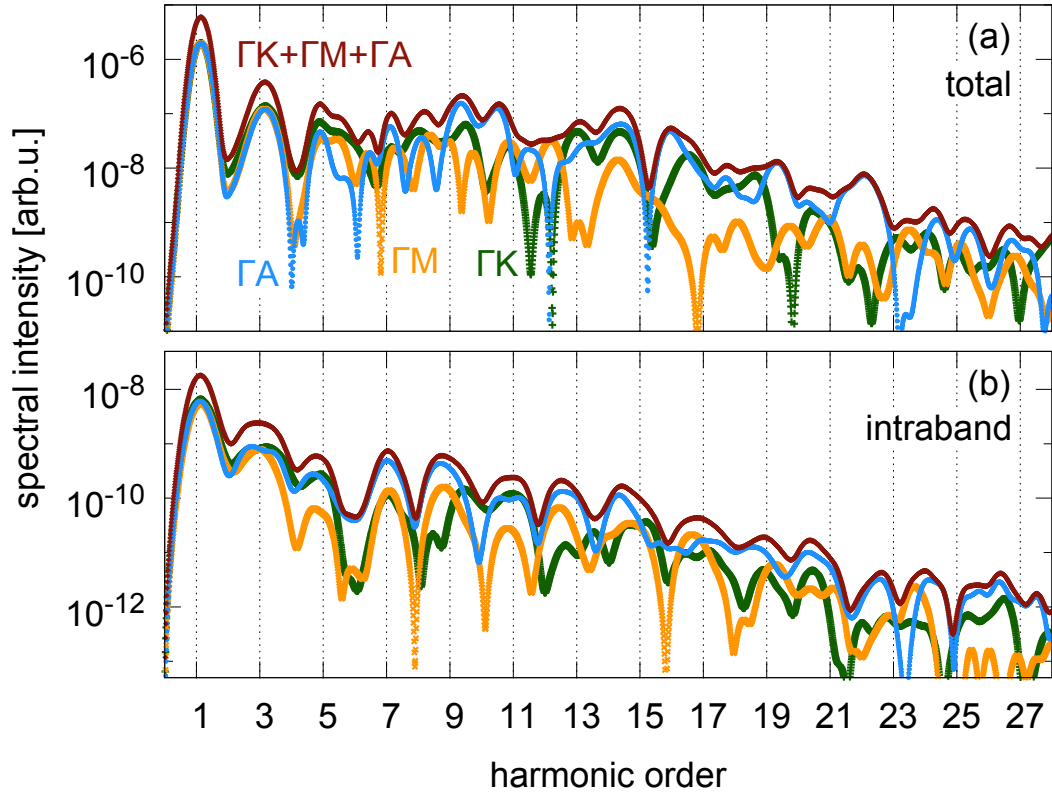


Figure 24: Total (a) and intraband (b) HHG spectra induced in  $\text{SiO}_2$  by the laser pulse given in Fig. 23a for laser polarizations parallel to  $\Gamma K$  (green),  $\Gamma M$  (orange), and  $\Gamma A$  (blue), and the incoherent superposition of all three (brown). No decoherence is imposed ( $\tau_{\text{dec}} = \infty$ ). For the Fourier transform of the current, we use a Gaussian window function with a width of  $\sigma_t = 2$  fs centered around  $\tau_0 = 7$  fs.

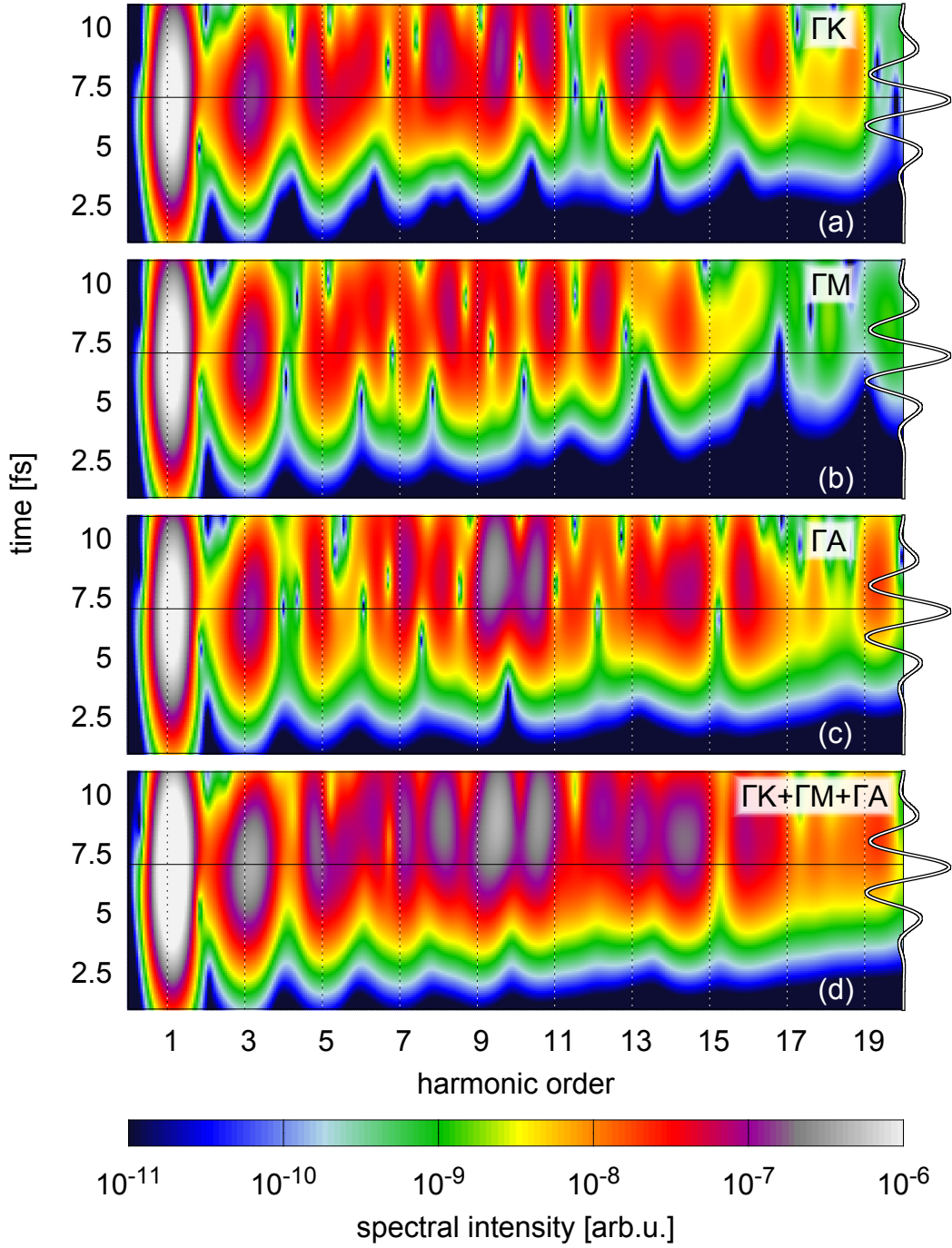


Figure 25: Time-frequency analysis (with high frequency resolution) of the emitted total intensity induced in  $\text{SiO}_2$  by the laser pulse given in Fig. 23a for laser polarizations parallel to  $\Gamma K$  (a),  $\Gamma M$  (b), and  $\Gamma A$  (c), and the incoherent superposition of all three (d) ( $\tau_{\text{dec}} = \infty$ ). For the Gabor transform we choose a Gaussian window function with a width of  $\sigma_t = 2$  fs. On the right hand side the time dependence of the external electric field is shown. The spectral intensities along the horizontal black lines correspond to the spectra shown in Fig. 24a.

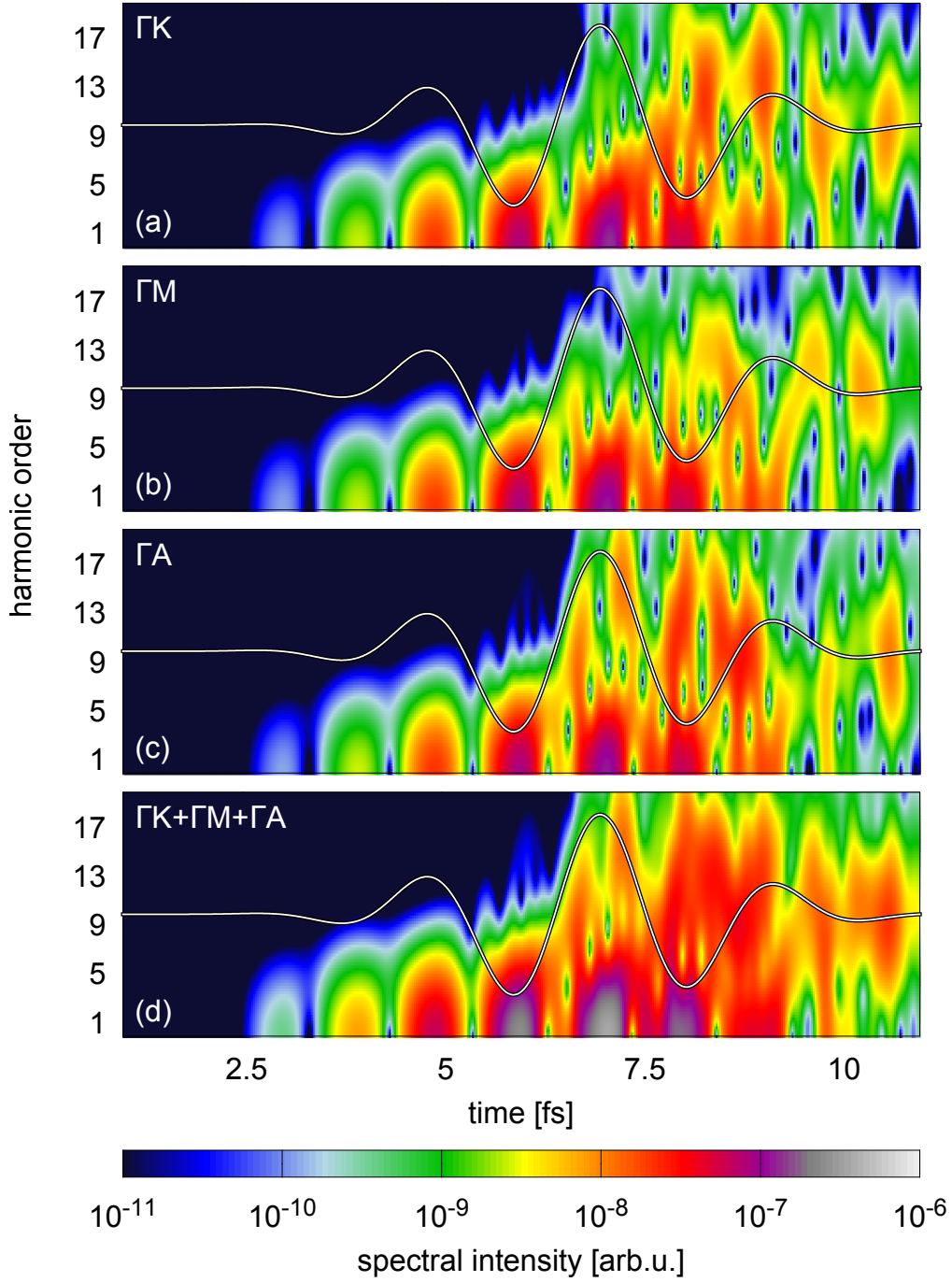


Figure 26: Time-frequency analysis (with high time resolution) of the emitted total intensity induced in  $\text{SiO}_2$  by the laser pulse given in Fig. 23a for laser polarizations parallel to  $\Gamma K$  (a),  $\Gamma M$  (b), and  $\Gamma A$  (c), and the incoherent superposition of all three (d) ( $\tau_{\text{dec}} = \infty$ ). For the Gabor transform of the time derivative of the induced current density, we choose a Gaussian window function with a width of  $\sigma_t = 0.1$  fs. The solid lines show the time dependence of the external electric field.

### 4.3 Conclusions and outlook

We have studied the HHG spectra from  $\alpha$ -quartz induced by a strong and short laser pulse for three different polarization directions (parallel to  $\Gamma K$ ,  $\Gamma M$ , and  $\Gamma A$ ). According to our TDDFT simulation (so far without decoherence<sup>11</sup>, damping, or propagation) and in contradiction with Luu et al. [2], polarization parallel to  $\Gamma M$  gives the least important contribution to the total as well as intraband spectra. Furthermore, the total spectrum is dominated by interband contributions with the intraband spectrum weaker by more than 2 orders of magnitude compared to the total spectrum.

With the calculated spectrum at high frequencies dominated by interband coherences, the first step for future investigations will be the implementation of decoherence in the TDDFT simulation also for  $\text{SiO}_2$ . This will increase the number of excited carriers and therefore enhance the intraband currents leading to a modified ratio between the intensities of inter- and intraband harmonics. We do not expect, however, the intraband contribution to dominate the total HHG spectra.

---

<sup>11</sup>The implementation of decoherence is so far only applicable to numerically cheap systems such as diamond (see discussion in Sec. 3.3.4).



## 5 Pump probe study of HHG

### 5.1 Motivation

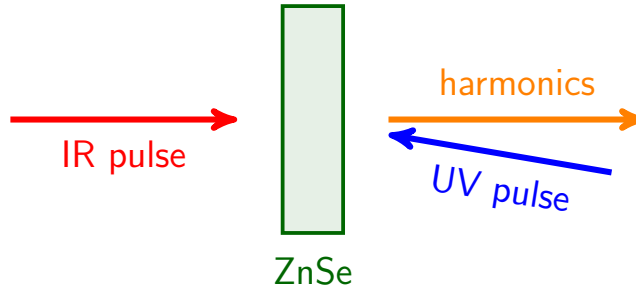


Figure 27: Illustration of the experimental setup: counter propagating UV pump and IR probe pulses irradiate a 0.5 mm thick ZnSe sample.

Recently, Baudisch et al. investigated the effect of a UV pump pulse on the HHG spectrum emitted from ZnSe driven by an IR probe pulse [5] (Fig. 27). First, a reference spectrum generated by the IR pulse alone ( $\hbar\omega_L = 0.4$  eV photon energy, 80 fs FWHM pulse duration, and  $I_{\max} \sim 10^{12}$  W/cm<sup>2</sup> peak intensity) was measured. Unfortunately, the 7<sup>th</sup> harmonic and a strong fluorescence peak close to the gap energy ( $E_{\text{gap}} = 2.71$  eV [?]) overlap. Therefore and due to limitations of the detector, well-defined reference values only for the 5<sup>th</sup>, 9<sup>th</sup>, and 11<sup>th</sup> harmonic intensities are available. Then, Baudisch et al. varied delay times between UV pump ( $\hbar\omega_L = 3.1$  eV ( $> E_{\text{gap}}$ ), 150 fs FWHM pulse duration, and  $I_{\max} = 2.6 \times 10^9$  W/cm<sup>2</sup>) and IR probe pulses from  $T_{\text{delay}} = 0$  ( $\hat{=}$  overlap) to 95 ps and studied the changes of individual harmonics as a function of  $T_{\text{delay}}$ . Apart from fluorescence and odd harmonic peaks overlapping pulses generate also sidebands. For temporally clearly separated pump and probe pulses an enhanced 5<sup>th</sup> harmonic (+12%) below  $E_{\text{gap}}$  and decreased 9<sup>th</sup> (-42%) and 11<sup>th</sup> (-8%) harmonics above  $E_{\text{gap}}$  were observed. Changes of the HHG spectrum decay on the 10 ps scale (Fig. 28). This was interpreted as the excitation of long-lived excitonic states close to the bottom of the conduction band of ZnSe (lifetime down to a few ps for small structures [18]) serving as initial state for the IR-HHG shifting the weight

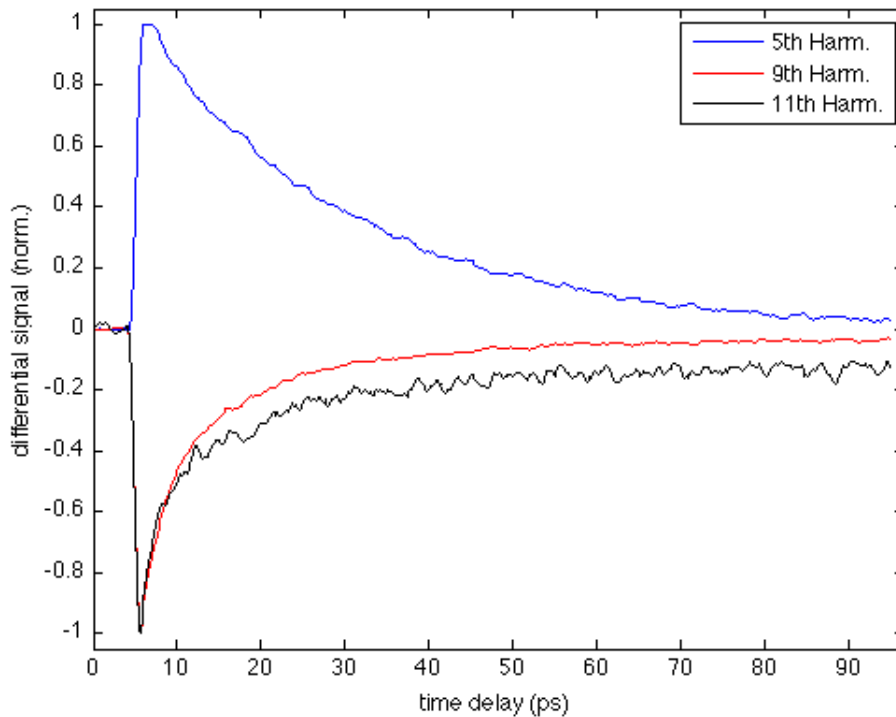


Figure 28: Normalized enhancement of the 5<sup>th</sup> (blue) and decreases of the 9<sup>th</sup> (red) and 11<sup>th</sup> (black) harmonic intensities as functions of the time delays between pump and probe pulses measured by Baudisch et al. [5].

from interband to intraband generation. The measurements suggest that harmonic peaks below the gap energy were enhanced whereas harmonics above were decreased due to the pump pulse in line with the interpretation of an enhanced intraband HHG. To test this assumption, we investigate the influence of initial conduction band population on the intensity of various harmonic peaks in our TDDFT simulation.

## 5.2 Mid-IR pulse on ZnSe

### 5.2.1 Simulated crystal

Before starting the simulation pseudopotentials for Zn and Se were created, an appropriate unit cell constructed, and convergence studies were performed. From these pre-studies the following parameter set emerged: ZnSe has a zincblende structure i.e. diamond structure with 2 atomic species and lattice constant 10.71 a.u. [11]. It can be

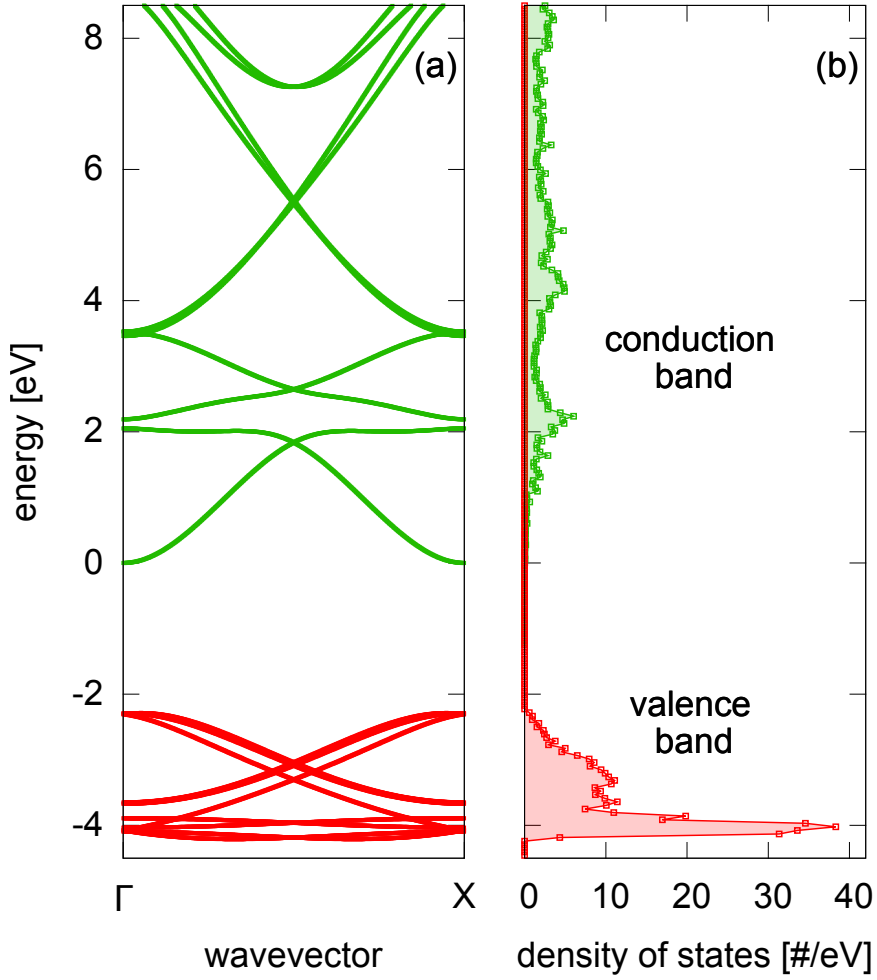


Figure 29: Simulated valence (red) and conduction (green) band structure (a) and density of states (b) of the ZnSe crystal.

discretized in a cuboid  $7.57 \times 7.57 \times 10.71$  a.u.<sup>3</sup> unit cell with step size  $\Delta x_i \simeq 0.28$  a.u. in real space and  $\Delta k_i \simeq 0.05$  a.u. in reciprocal space (with  $i = 1, 2, 3$ ). Again, we use a time step of  $\Delta t = 0.02$  a.u.

In the simulation Zn and Se have 12 (Zn[4s<sup>2</sup>3d<sup>10</sup>]) and 6 (Se[4s<sup>2</sup>4p<sup>4</sup>]) active electrons leading to 18 doubly occupied orbitals in a unit cell consisting of 2 Zn and 2 Se atoms. The inner shell electrons are frozen and included in the norm-conserving pseudopotentials. For the XC functional we apply the TBmBJ potential with  $c = 1.8$  [17] resulting in a band gap energy of  $E_{\text{gap}} = 2.3$  eV (LDA value:  $E_{\text{gap}} = 1.4$  eV). The resulting band structure, density of states, and dielectric function are shown in

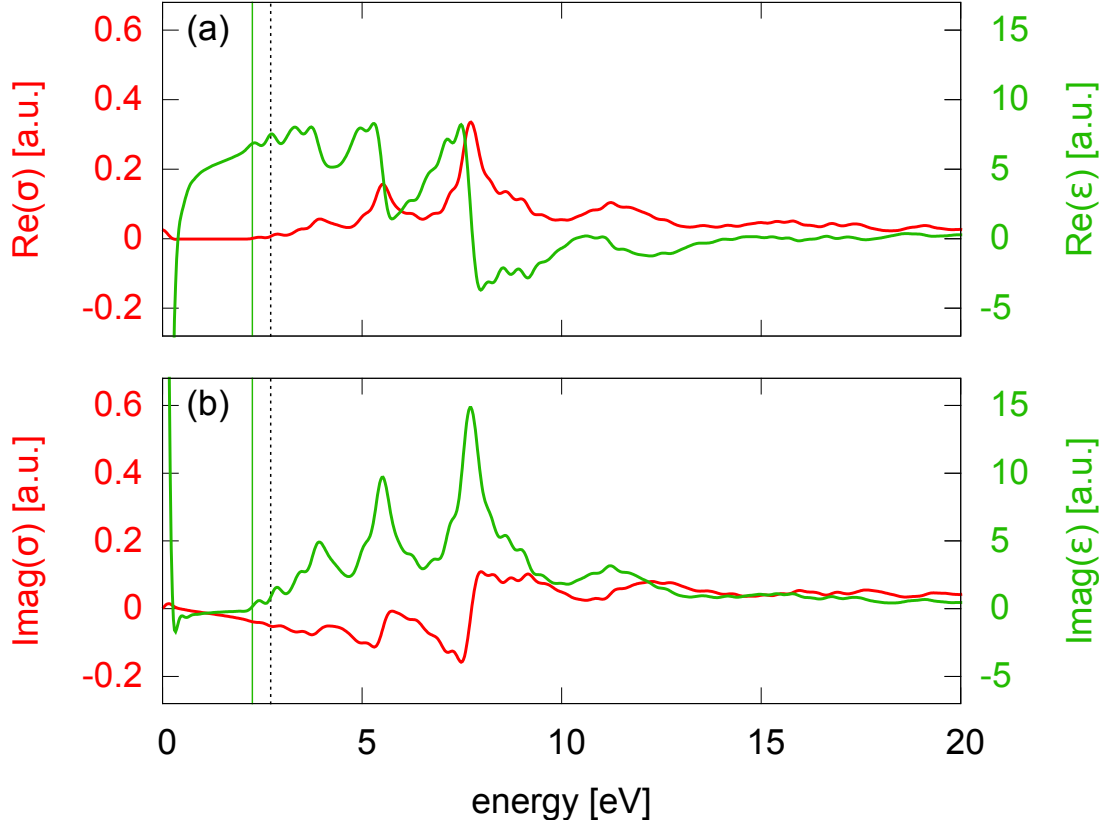


Figure 30: Real (a) and imaginary (b) parts of the conductivity (red) and the dielectric function (green) of ZnSe computed in a response calculation. The vertical lines indicate experimental (dashed black) and simulated (solid green) band gaps.

Figs. 29 and 30. Excitonic states are not available in our TDDFT system but will be replaced by an initial occupation of the lowest conduction band state.

### 5.2.2 Original and modified spectra

First, we need an estimate for the percentage of conduction band electrons after irradiation by the UV pump pulse. Therefore, we send a pulse polarized along the  $\Gamma$ -X direction and corresponding to the experimental parameters ( $\hbar\omega_L = 3.1$  eV and  $I_{\max} = 2.6 \times 10^9$  W/cm<sup>2</sup>) onto the ZnSe unit cell. We use a shorter pulse than in experiment (duration of 40 fs with a  $\cos^4$ -envelope) in order to keep the numerical effort acceptable. After irradiation 0.0036% of the 36 electrons in the unit cell remain in the conduction band. Taking account of the longer duration of the experimental

pulse (increase by a factor of about 7.5) and decoherence effects (leading to enhanced excitation assumed to give rise to a factor of  $\lesssim 2$ ), we estimate at most about 0.05% conduction band population after conclusion of the blue pulse. This is used as an upper limit for the initial conduction band population in the subsequent time dependent simulation. As a first rough approximation for excitons being localized states, we distribute the initial excited population equally within the Brillouin zone into the lowest conduction band level.

We aim at simulating the effect of the pump pulse for two different delay times between pump and probe pulses by studying the following 3 cases in detail: initially no electron in the conduction band (starting from the ground state), 0.01 ( $\hat{=} n^{\text{exc}} = 0.028\%$  conduction band population), and 0.02 ( $\hat{=} n^{\text{exc}} = 0.056\%$ ) out of 36 active electrons in the conduction band. For the TDDFT simulation we stick to the experimental parameters ( $\hbar\omega_L = 0.4$  eV and  $I_{\text{max}} = 10^{12}$  W/cm<sup>2</sup>) but choose a slightly shorter pulse (duration of 103 fs with a  $\cos^6$ -envelope; see Fig. 31a) polarized along the  $\Gamma$ -X direction. Initial excited carriers ensure enhanced conduction band population also at later times (Fig. 31d) directly leading to enhanced intraband current densities (Fig. 31c). Therefore, the total current is phase-shifted and, especially before the field maximum, increased due to initial excited carriers (Fig. 31b). Furthermore, the enhanced intraband current leads to an enhancement of all harmonics in the intraband spectrum (Fig. 32b). Also wide ranges of the total spectrum are increased at least partially caused by the earlier starting emission of radiation. Rather surprisingly, we observe destructive interference leading to decreasing intensity of the 3<sup>rd</sup> harmonic for increasing initial conduction band population (Figs. 32a and 33). The origin of this destructive interference will be subject of future investigations.

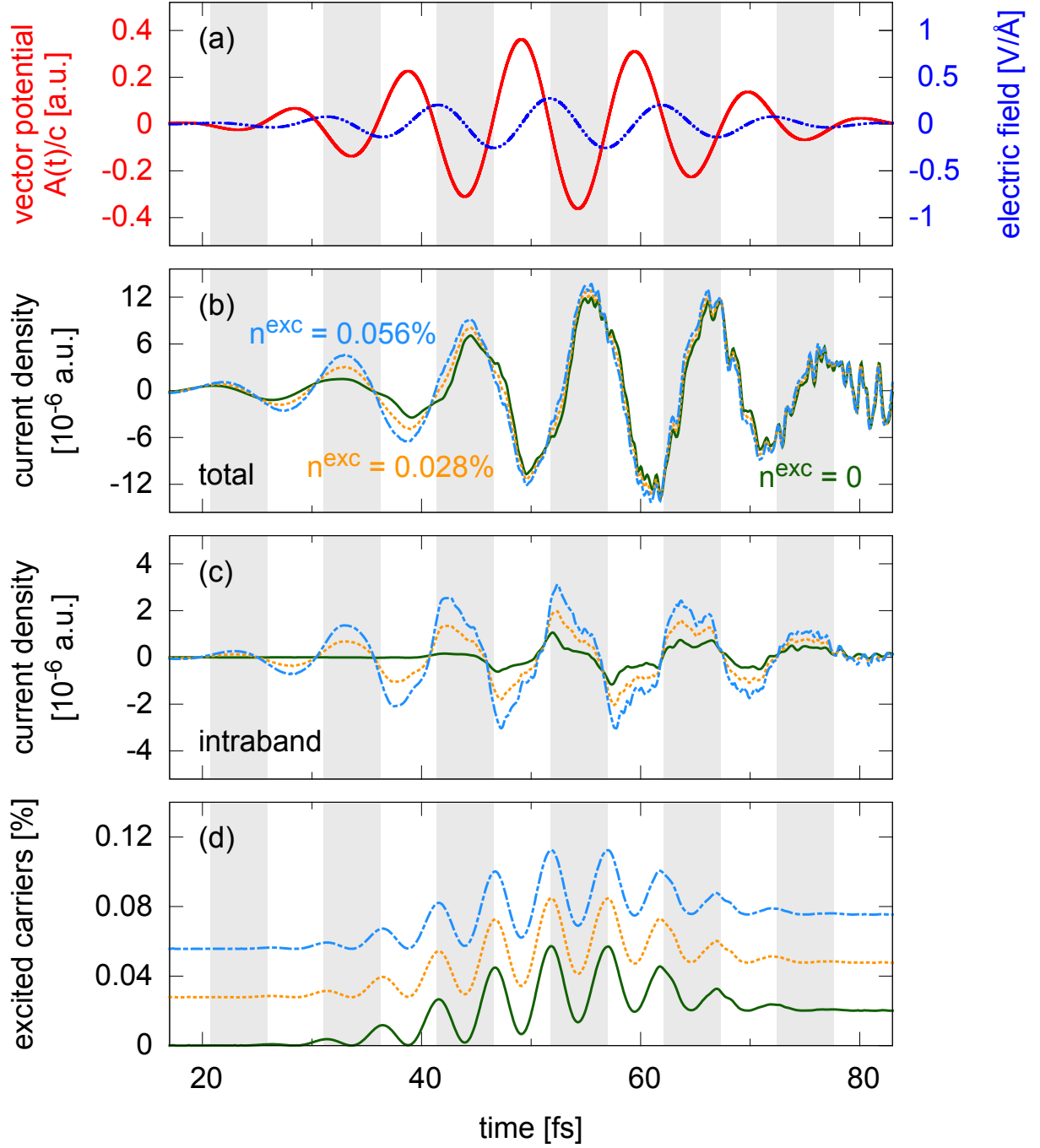


Figure 31: (a) Electric field with a  $\cos^6$ -envelope, peak intensity  $I_{\max} = 10^{12}$  W/cm<sup>2</sup>,  $\hbar\omega_L = 0.4$  eV, and  $\phi_{\text{CE}} = 0$  (blue) and the corresponding input vector potential  $\mathbf{A}(t)/c$  (red). (b-d) Induced total (b) and intraband (c) current densities and percentage of conduction band electrons (d) where initially (at  $t = 0$  fs) 0 (green), 0.01 (orange), and 0.02 (blue) out of 36 electrons in the ZnSe unit cell are excited ( $\tau_{\text{dec}} = \infty$ ).

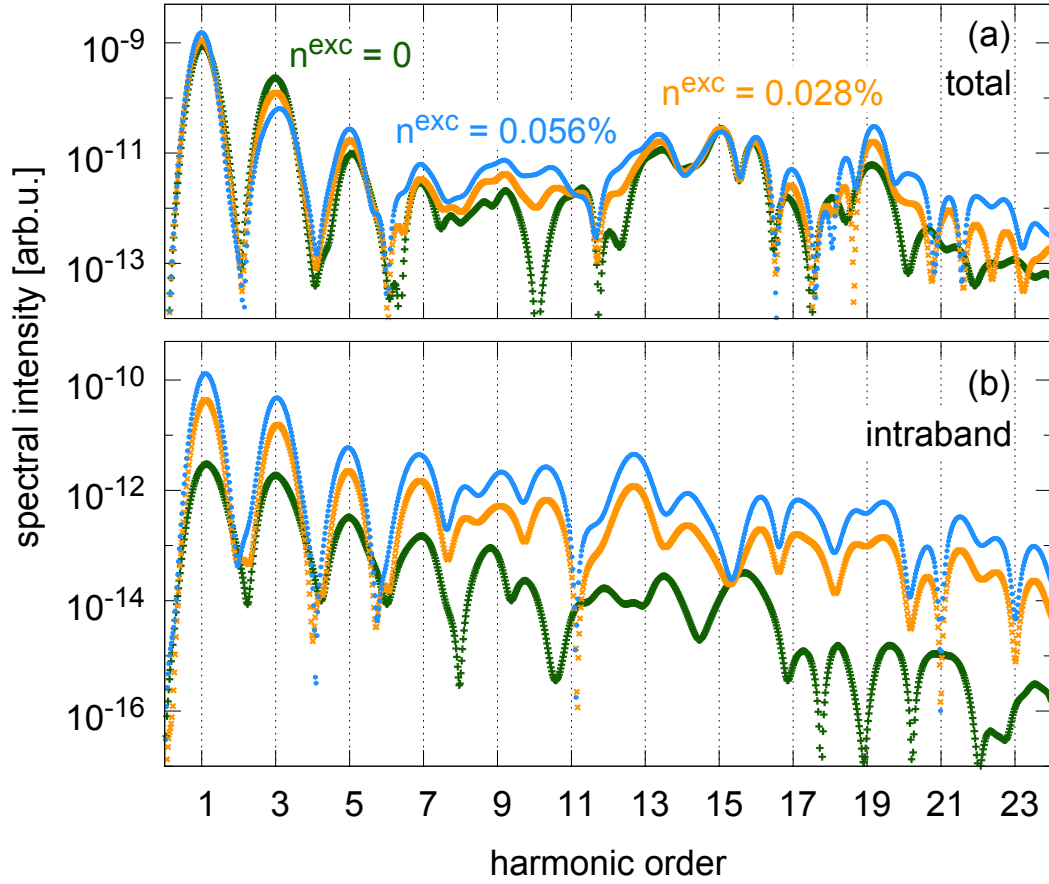


Figure 32: Total (a) and intraband (b) HHG spectra induced in ZnSe by the laser pulse given in Fig. 31a for initially 0 (green), 0.01 (orange), and 0.02 (blue) out of 36 electrons in the conduction band. No decoherence is imposed ( $\tau_{\text{dec}} = \infty$ ). For the Fourier transform of the current, we use a Gaussian window function with a width of  $\sigma_t = 6$  fs centered around  $\tau_0 = 45$  fs.

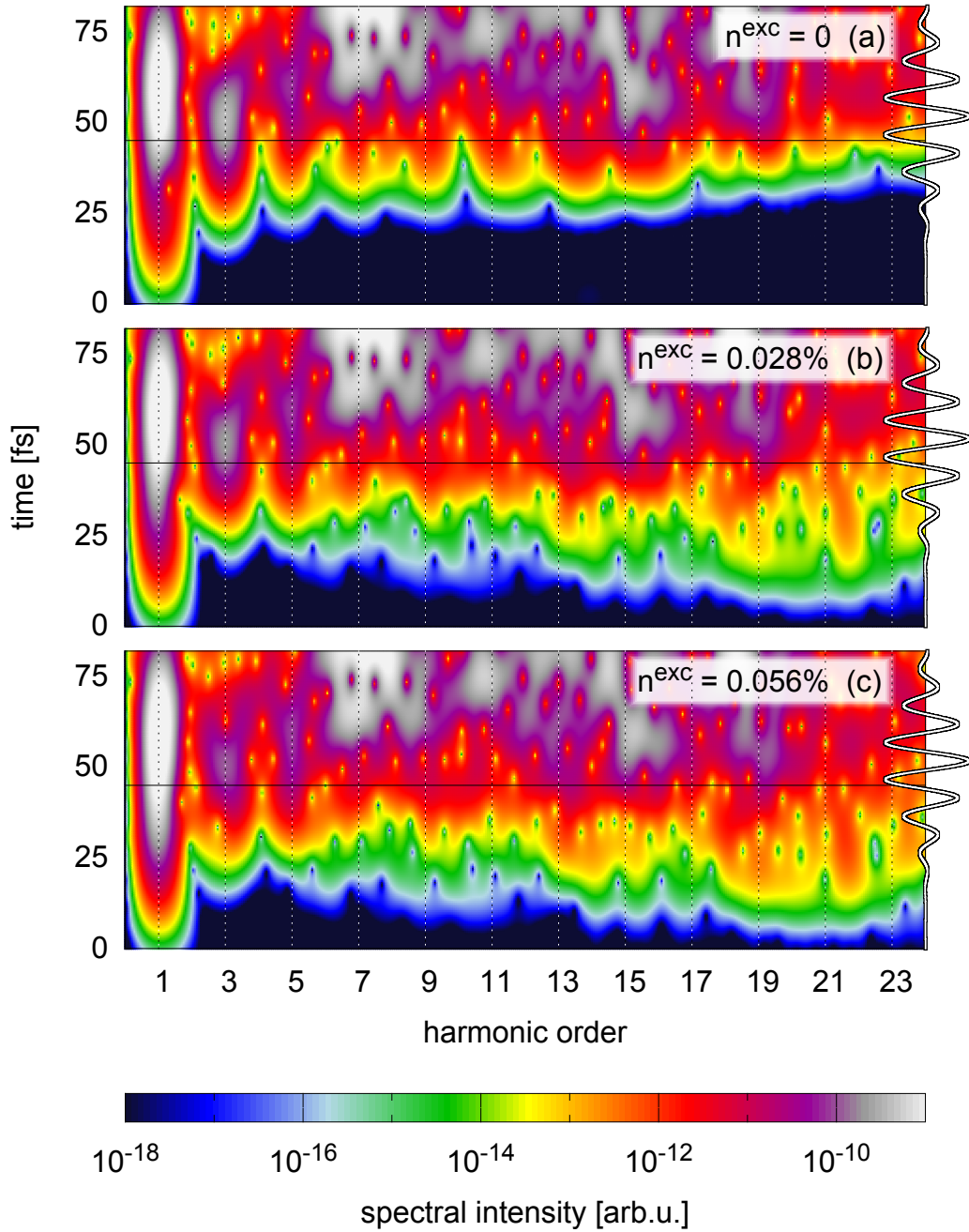


Figure 33: Time-frequency analysis of the emitted total intensity induced by the laser pulse given in Fig. 31a where initially 0 (a), 0.01 (b), and 0.02 (c) out of 36 electrons in the ZnSe unit cell are excited ( $\tau_{\text{dec}} = \infty$ ). For the Gabor transform we choose a Gaussian window function with a width of  $\sigma_t = 6$  fs. On the right hand side the time dependence of the external electric field is shown. The spectral intensities along the horizontal black lines correspond to the spectra shown in Fig. 32a.

### 5.3 Near-IR pulse on diamond

In order to better understand how initial carrier densities influence HHG spectra, we choose diamond (the numerically cheap crystal we are most familiar with), a higher initial carrier density (up to 1 out of 16 active electrons in the conduction band), and a higher peak intensity as well as photon energy ( $I_{\max} = 2 \times 10^{13} \text{ W/cm}^2$ ,  $\hbar\omega_L = 1.55 \text{ eV}$ ) for the input pulse (Fig. 34a) polarized along the  $\Gamma$ -X direction. The test system diamond also allows to study the influence of decoherence on the results. Furthermore, even for very high initial conduction band densities (up to 1 out of 16 electrons in the unit cell) the simulation is still numerically stable.

Here, we present 3 cases in detail: initially 0 (starting from the ground state), 0.2 ( $\hat{=} n^{\text{exc}} = 1.25\%$  conduction band population), and 1 ( $\hat{=} n^{\text{exc}} = 6.25\%$ ) out of 16 active electrons in the conduction band. As expected, higher initial carrier densities lead to strongly enhanced intraband currents increasingly controlling the total currents with and without decoherence. Surprisingly, the induced current density reaches its maximum before the field maximum (Fig. 34b-d). This finding demands for a more detailed analysis of the induced current density and all its contributions (from various bands and/or  $\mathbf{k}$ -points) which will be subject of future investigations.

As for ZnSe, the enhanced initial CB occupation results in enhanced intraband HHG at all orders (Figs. 35b, 36b). Still, interband HHG dominates for larger orders  $n \gtrsim 9$  leaving the total HHG spectrum (apart from the reduced 11<sup>th</sup> and enhanced 13<sup>th</sup> harmonics) almost unchanged at higher energies. For harmonic order  $n \leq 7$  the total intensities of the harmonics increase with increasing initial CB occupation with the notable exception of the 1<sup>st</sup> harmonic. The intensity of the 1<sup>st</sup> harmonic decreases up to a critical initial CB population  $n^{\text{exc, crit}}$  and increases again for further increasing  $n^{\text{exc}}$  (Figs. 35a, 37). This can be understood as follows: the induced current density changes its character from interband-like, i.e., in phase with the external vector potential (see Sec. 2.2.1) to intraband dominated with a phase shift of  $\pi$  relative to the vector potential with increasing  $n^{\text{exc}}$ . The minimum of the 1<sup>st</sup> harmonic is caused

by equally strong first-order inter- and intraband-like current density components. When we account for decoherence which, again, “clears up” the spectrum, the  $n^{\text{exc}}$ -dependent reduction of the 1<sup>st</sup> harmonic is not observed for the simulated values of  $n^{\text{exc}}$  but is expected at lower initial CB densities  $n_{\tau_{\text{dec}}=2\text{fs}}^{\text{exc, crit}} < n_{\tau_{\text{dec}}=\infty}^{\text{exc, crit}}$  since CB occupation is enhanced by decoherence. However, apart from the special case of the 1<sup>st</sup> harmonic a comparison between the standard calculation ( $\tau_{\text{dec}} = \infty$ ; Fig. 35) and a calculation allowing for decoherence ( $\tau_{\text{dec}} = 2$  fs; Fig. 36) gives very similar modifications of harmonic intensities due to initial excited carriers.

## 5.4 Conclusions and outlook

For our simulations of pump-probe experiments we could not derive a general rule for the enhancement or decrease of individual harmonics within or above the band gap. Special features of the potential landscape resulting in unique dispersion relations strongly influence the results. Therefore, the modification of individual harmonics due to initial excited carriers sensitively depends on material properties and polarization direction. Since the experimental polarization direction is unknown and, therefore, most likely does not coincide with the polarization direction in the simulation, we cannot accurately reproduce the measured results.

So far, we have observed but have not fully understood the enhancement or reduction of individual harmonics. Therefore, a more detailed splitting of the induced current into all its contributions will be the first step for future investigations. This will open the pathway to identifying bands and probably  $\mathbf{k}$ -points dominantly contributing to individual harmonics. From studying the phase relation of the corresponding induced currents, we will get a better idea of the occurring constructive and destructive interference processes.

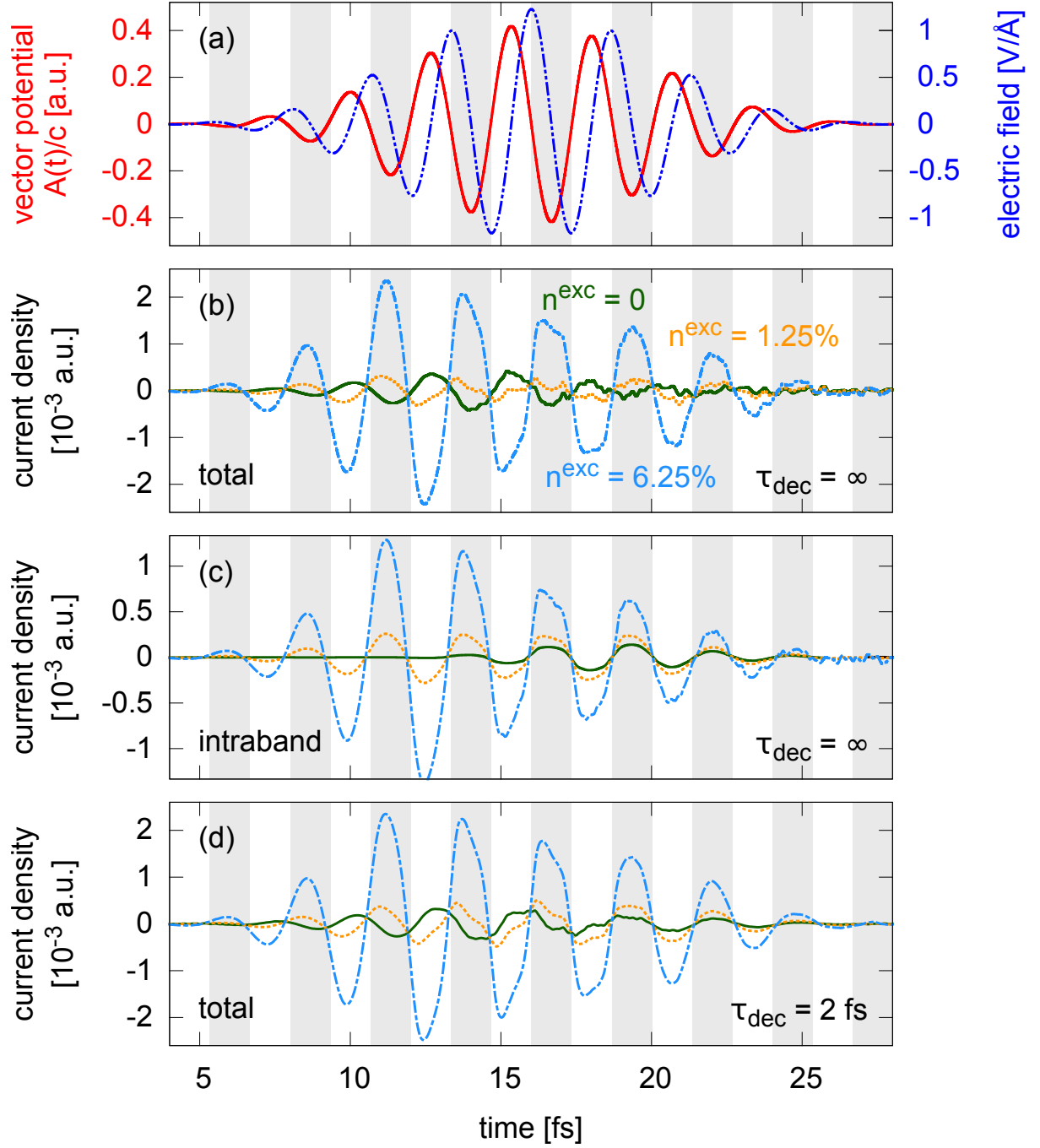


Figure 34: (a) Input vector potential  $\mathbf{A}(t)/c$  (red) and corresponding electric field (blue) with a  $\cos^6$ -envelope, peak intensity  $I_{\text{max}} = 2 \times 10^{13}$  W/cm<sup>2</sup>,  $\hbar\omega_L = 1.55$  eV, and  $\phi_{\text{CE}} = 0$ . Induced total current density along the laser polarization direction (b) and intraband contribution without decoherence (c) for initial  $n^{\text{exc}} = 0$  (green), 0.2 (orange), and 1 (blue) out of 16 electrons in the diamond unit cell. (d) Same as panel (b) but with decoherence time  $\tau_{\text{dec}} = 2$  fs.

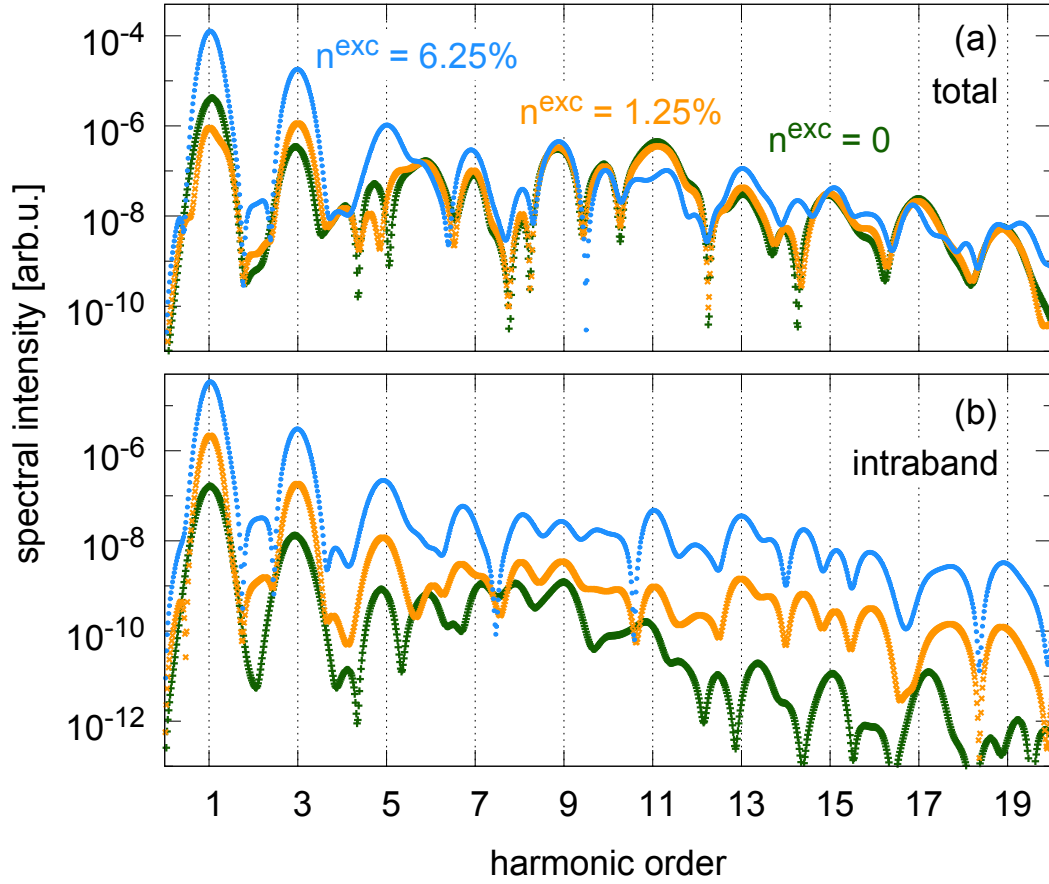


Figure 35: Total (a) and intraband (b) HHG spectra induced in diamond by the laser pulse of Fig. 34a for initially 0 (green), 0.2 (orange), and 1 (blue) out of 16 electrons in the conduction band without decoherence ( $\tau_{\text{dec}} = \infty$ ). For the Fourier transform of the current, we use a Gaussian window function with a width of  $\sigma_t = 2$  fs centered around  $\tau_0 = 15$  fs .

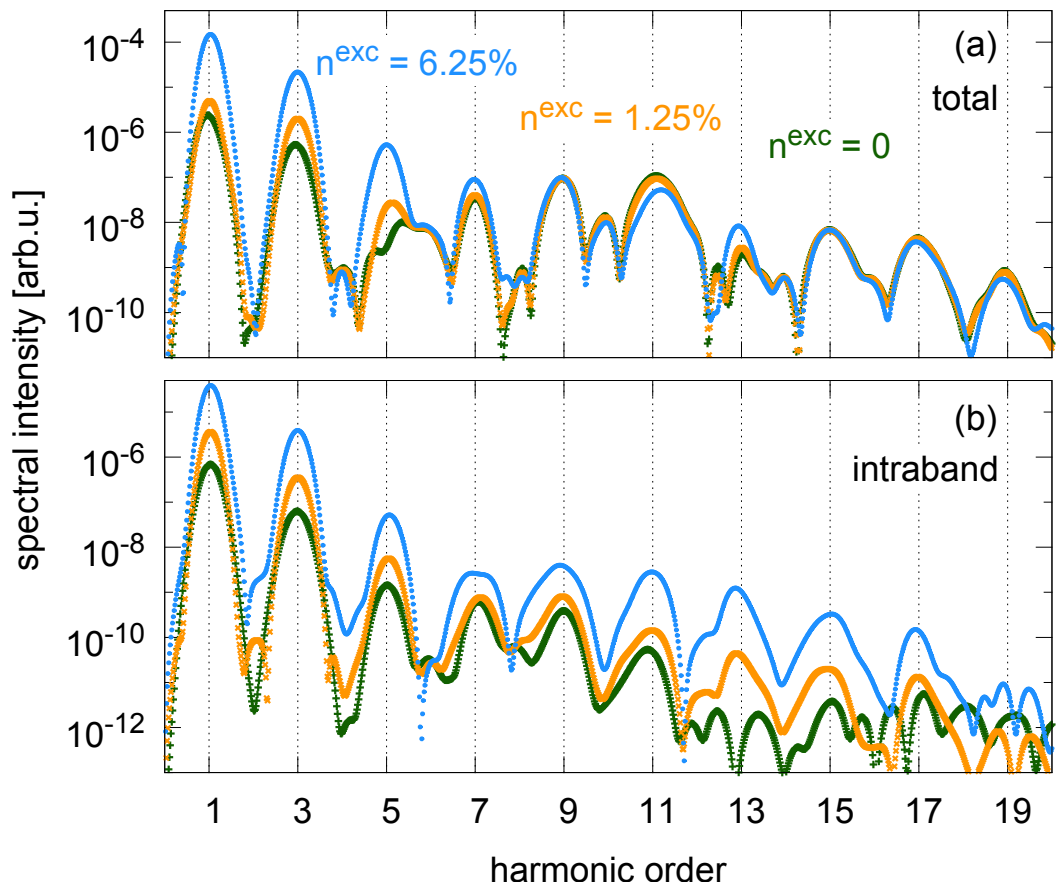


Figure 36: Same as Fig. 35 but for a decoherence time of  $\tau_{\text{dec}} = 2$  fs.

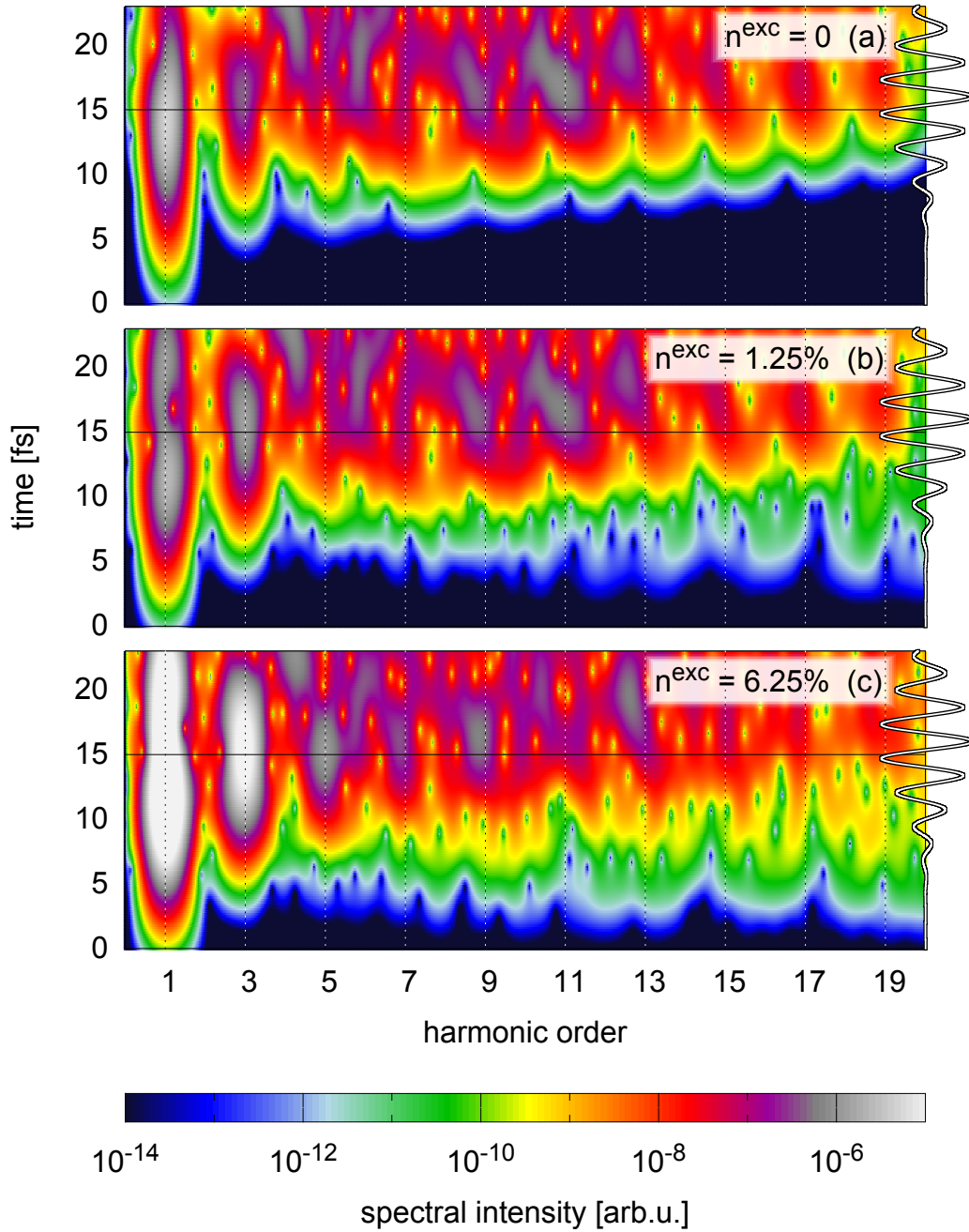


Figure 37: Time-frequency analysis of the emitted total intensity induced by the laser pulse given in Fig. 34a for an initial excitation of 0 (a), 0.2 (b), and 1 (c) out of 36 electrons in the diamond unit cell ( $\tau_{\text{dec}} = \infty$ ). For the Gabor transform we choose a Gaussian window function with a width of  $\sigma_t = 2$  fs. On the right hand side the time dependence of the external electric field is shown. The spectral intensities along the horizontal black lines correspond to the spectra shown in Fig. 35a.

## 6 Conclusions and outlook

When describing the interaction of strong and short laser pulses with crystalline solids, one of the most elaborate and reliable methods is TDDFT. Nevertheless, several aspects of the true many-body problem are not sufficiently taken into account which still leaves room for improvements. Within this diploma thesis both methodological aspects in terms of extending and improving the available TDDFT approach (Secs. 2, 3) and its practical applications inspired by recent experiments (Secs. 4, 5) were studied. While Yabana et al. [12] have achieved great success in including propagation effects via treating the coupled dynamics of electrons and electromagnetic fields, we focused on different approaches introducing dissipative and coherence-loss effects in the TDDFT simulation. As especially the implementation of decoherence shows very promising first results, future investigations aim at extending this method and making it applicable to all systems finally arriving at a combined treatment of decoherence and propagation effects within one simulation.

One of the observables that can be measured in experiments as well as extracted from the TDDFT simulation is the high harmonic radiation emitted from crystalline insulators irradiated by laser pulses. Typically, theoretical investigations of HHG from solids are based on solving the optical Bloch equations for 1D and two bands [2] which is numerically much less expensive than TDDFT simulations. However, from studying the directional dependence of HHG in  $\alpha$ -quartz (Sec. 4), we find discrepancies between both approaches indicating that one line taken from the 3-dimensional band structure might be an insufficient description of a solid.

While HHG from atoms is already reasonably well understood, a simple model convincingly describing HHG from solids is still missing. Indeed, there is ongoing strong debate on the relative roles of inter- and intraband contributions [1, 2]. Having succeeded in the separation of the conduction band current in our TDDFT simulation (Sec. 2), we have reason to believe that in most cases interband HHG is much more intense than intraband HHG. In order to better understand HHG from solids and

also the modification of individual harmonics due to initial excited carriers which sensitively depends on material properties (Sec. 5), future investigations will focus on the separation of the induced current density into contributions from individual bands (i.e., dispersion relations). We will aim at identifying less and more important regions of the band structure for the generation of individual harmonics. Furthermore, we will try to get a better picture for solid HHG not only in reciprocal space but also in real space by splitting the microscopic current densities and changes in the charge density into components associated with individual harmonics.

## 7 Acknowledgments

This diploma thesis as it is would not have been possible without the support of several people I would like to appreciate. Some time ago it was Christoph Lemell who attracted me to the group of Theoretical Quantum Dynamics. Since then he has not only shown admirable patience in numerous discussions but also repeatedly found the right words in many situations. Thank you for taking care of all kinds of problems and for believing in my abilities more than I do. Georg Wachter brought me into the topic of laser-matter interactions where he has left a solid foundation of knowledge. I am very grateful for ongoing help and advice from your side although you have already left the world of science. Many thanks go to Joachim Burgdörfer who has enabled me to gain scientific experience abroad and from whose expertise I have greatly benefited many times. Due to his constant interest in my progress I have been motivated to go on again and again. Thank you for new perspectives on problems I had to deal with. I am very grateful to Kazuhiro Yabana and (former) members of his group for developing and providing the TDDFT package I have used throughout my thesis. Special thanks go to Shunsuke Sato, Xiao-Min Tong, and Kazuhiro Yabana who warmly welcomed me at the University of Tsukuba, gave me insight into the Japanese culture and made my stay in Japan a memorable time. Thank you very much for many interesting and instructive discussions and a pleasant ongoing collaboration. Furthermore, I am very grateful to Matthias Baudisch, Hugo Pires, and Jens Biegert for providing measurement data serving as a benchmark for the simulation results.

During my studies I had the chance to meet many interesting people resulting in a beautiful and enlightening time rich in variety. I am very grateful for a few close friendships that have arisen. Many thanks go to various people from the Institute for Theoretical Physics for being incredibly helpful at any time (especially, I am very grateful to my office colleague, Florian Libisch, for countless times of support with computer-, physics-, and other problems), for providing a never-ending source of

chocolate and other sweets, and for initiating lots of events and activities both inside and outside the university. Thanks for numerous interesting discussions.

Last but not least I want to thank my family and non-physicist friends who steadily reminded me of the diversity of life and the importance of finding the right balance in life. I am very grateful to my parents for material as well as financial support. Special thanks go to my mother and brother for trying to alleviate all kinds of problems.

## References

- [1] G. VAMPA, C. R. McDONALD, G. ORLANDO, D. D. KLUG, P. B. CORKUM, and T. BRABEC, *Phys. Rev. Lett.* **113**, 073901 (2014).
- [2] T. T. LUU, M. GARG, S. Y. KRUCHININ, A. MOULET, M. T. HASSAN, and E. GOULIELMAKIS, *Nature* **521**, 498 (2015).
- [3] K. YABANA, Y. SHINOHARA, T. OTOBE, J.-I. IWATA, and G. F. BERTSCH, First-principles calculations for laser induced electron dynamics in solids, in *Advances in Multi-Photon Processes and Spectroscopy*, volume 21, chapter 6, World Scientific, 2014.
- [4] G. WACHTER, S. A. SATO, I. FLOSS, C. LEMELL, X.-M. TONG, K. YABANA, and J. BURGDÖRFER, *New Journal of Physics* **17**, 123026 (2015).
- [5] M. BAUDISCH, H. PIRES, and J. BIEGERT, private communication.
- [6] N. TROULLIER and J. L. MARTINS, *Phys. Rev. B* **43**, 1993 (1991).
- [7] D. D. JOHNSON, *Phys. Rev. B* **38**, 12807 (1988).
- [8] G. KRESSE and J. FURTHMÜLLER, *Phys. Rev. B* **54**, 11169 (1996).
- [9] W. V. HOUSTON, *Phys. Rev.* **57**, 184 (1940).
- [10] J. JACKSON and K. MÜLLER, *Klassische Elektrodynamik*, de Gruyter, 2002.
- [11] D. LIDE, *CRC Handbook of Chemistry and Physics*, 85th Edition, CRC Press, 2004.
- [12] K. YABANA, T. SUGIYAMA, Y. SHINOHARA, T. OTOBE, and G. F. BERTSCH, *Phys. Rev. B* **85**, 045134 (2012).
- [13] D. NEUHAUSER and K. LOPATA, *J. Chem. Phys.* **129**, 134106 (2008).

- [14] V. SMEJKAL, *An Investigation of Drude-like Friction Models for TDDFT*, project thesis, Vienna University of Technology, Institute for Theoretical Physics, 2016.
- [15] M. SCHULTZE, E. M. BOTHSCHAFTER, A. SOMMER, S. HOLZNER, W. SCHWEINBERGER, M. FIESS, M. HOFSTETTER, R. KIENBERGER, V. APALKOV, V. S. YAKOVLEV, M. STOCKMAN, and F. KRAUSZ, *Nature* **493**, 75 (2013).
- [16] G. WACHTER, *Simulation of condensed matter dynamics in strong femtosecond laser pulses*, PhD thesis, Vienna University of Technology, Institute for Theoretical Physics, 2014.
- [17] F. TRAN and P. BLAHA, *Phys. Rev. Lett.* **102**, 226401 (2009).
- [18] T. STEINER, M. L. W. THEWALT, and R. N. BHARGAVA, *Sol. Stat. Comm.* **56**, 933 (1985).